Quaternary Science Reviews
July 2018, Volume 191 Pages 57-72
https://doi.org/10.1016/j.quascirev.2018.05.007
https://archimer.ifremer.fr/doc/00440/55185/

Relative paleointensity (RPI) in the latest Pleistocene (10–45 ka) and implications for deglacial atmospheric radiocarbon

Channell J. E. T. [1, *], Hodell D. A. [2], Crowhurst S. J. [2], Skinner L. C. [2], Muscheler R. [3]

[1] Univ Florida, Dept Geol Sci, 241 Williamson Hall,POB 112120, Gainesville, FL 32611 USA.
[2] Univ Cambridge, Dept Earth Sci, Godwin Lab Palaeoclimate Res, Downing St, Cambridge CB2 3EQ, England.
[3] Lund Univ, Quaternary Sci, Dept Geol, Solvegatan 12, SE-22362 Lund, Sweden.

* Corresponding author : J. E. T. Channel, email address : jetc@ufl.edu

Abstract :

We report magnetic properties and relative paleointensity (RPI) proxies from a suite of 10 conventional piston cores and Kasten cores from the SW Iberian Margin collected during cruise JC089 of the RSS James Cook in August 2013. Mean sedimentation rates are in the 10–20 cm/kyr range. Age models were acquired by correlation of Ca/Ti and Zr/Sr XRF core-scanning data to L* reflectance from the Cariaco Basin that is, in turn, tied to the Greenland ice-core chronology. The natural remanent magnetization (NRM) is represented by a single magnetization component carried by a low-coercivity mineral (magnetite), although reflectance and bulk magnetic properties indicate the presence of a high-coercivity (hematitic) magnetic phase, possibly from eolian dust. The presence of fine-grained hematite means that the sediments are not ideal for RPI studies, however the detrital hematite does not appear to contribute to the NRM or anhysteretic remanent magnetization (ARM). In order to test the usefulness of the RPI data, we construct a stack of 12 RPI records from the SW Iberian Margin for the 0–45 ka interval and compare it with a stack of 12 globally distributed marine and lake records, chosen on the basis of mean sedimentation rates (>15 cm/kyr) and superior age models. The two stacks are similar, but different from published RPI stacks, particularly for the 10–30 ka interval, and imply a virtual axial dipole moment (VADM) high at ~15–18 ka followed by a drop in field strength from ~15 to 13 ka. A revised VADM estimate calculated from Greenland 10Be ice-core flux using a contemporary age model is remarkably consistent with the new overall RPI stack, based on Iberian Margin and global RPI records. The elevated atmospheric 14C levels of the last ice age cannot, however, be fully explained by this RPI stack although relative changes such as the long-term drop in atmospheric 14C from 30 to 15 ka are reproduced, supporting the hypothesis of a combined influence of production rate and ocean ventilation on 14C during the last ice age.

Highlights

► Revised view of relative paleointensity for the latest Quaternary (0–45 ka). ► Stack of SW Iberian and global relative paleointensity records for 0–45 ka. ► RPI stack consistent with recalculated ^{10}Be-based estimate of field intensity. ► Implications for the carbon cycle, ocean ventilation, and the “mystery interval”.

Keywords : Relative geomagnetic paleointensity, Latest Quaternary, SW Iberian margin, Carbon cycle, Ice-core Be-10, "Mystery interval", Atmospheric radiocarbon

1. Introduction

Consistent correlation of sedimentary relative paleointensity (RPI) proxies to oxygen isotope data over the last 1-2 Myrs (e.g., Channell et al., 2009; Xuan et al., 2016) has shown that RPI proxies in sediments can reflect the Earth's axial dipole (AD) field and therefore provide a signal suitable for global stratigraphic correlation. This conclusion is supported by the consistent picture of dipole field strength from RPI and from sedimentary $^{10}Be/^{9}Be$ ratios back to 850 ka (e.g., Simon et al., 2016). Because the strength of the AD field is an important control on atmospheric cosmogenic isotope production, RPI records have implications for the calibration of radiocarbon dates and for the carbon cycle including the apparent drop in atmospheric $\Delta^{14}C$ in the "mystery interval" at 17.5-14.5 kyr (Broecker and Barker, 2007).

The Holocene (0-11.5 ka) record of paleointensity has been modeled from archeomagnetic and lava-flow data (Korte et al., 2009, 2011; Pavon-Carrasco et al., 2014) indicating a pattern of AD field intensity changes characterized by a broad high in intensity at ~1-3 ka, preceded by a broad low in the 5-7 ka interval (Fig. 1b). Beyond the range of archeomagnetic data, latest Pleistocene (11.5-45 ka) sedimentary RPI data have been compiled into regional and global stacks (Laj et al., 2000, 2004; Stoner et al., 2002; Valet et al., 2005; Channell et al., 2009; Ziegler et al., 2011), but with little agreement

between stacks, or individual records, for the 10-30 ka interval (Fig. 1a). The poor consistency of sedimentary RPI data since the time of the Mono Lake (~34 ka) and Laschamp (~41 ka) excursions (Fig. 1a) is attributed to drilling disturbance in the uppermost few meters of recovered sediment sequences.

Absolute paleointensity data from volcanics have not contributed significantly to the paleointensity time-series for the 10-30 ka interval for several reasons: lava sequences are plagued by unknown time-gaps between flows, $^{40}Ar/^{39}Ar$ dating has poor precision for young (<40 ka) ages, scarcity of robust radiocarbon age control, and scatter in absolute paleointensity determinations when plotted versus age particularly for the 10-30 ka interval (e.g., Teanby et al., 2002; Pressling et al., 2006; Genevey et al., 2008; Laj et al., 2014).

Using models of cosmogenic nuclide production (Masarik and Beer, 1999), Muscheler et al. (2005) calculated the virtual axial dipole moment (VADM) corresponding to the flux of cosmogenic isotopes in ice cores for ^{36}Cl (Baumgartner et al., 1998; Wagner et al., 2000) and ^{10}Be (Yiou et al., 1997; Finkel and Nishiizumi, 1997). Estimates of atmospheric ^{14}C activity have been derived from independent age control on radiocarbon ages from stalagmites (Beck et al., 2001; Wang et al., 2001; Southon et al., 2011), corals (Fairbanks et al., 2005), lake varves (Bronk Ramsey et al*.,* 2012*)* and from the correlation of marine sediment cores to Greenland ice (Hughen et al., 2004; Peterson et al., 2000; Bard et al., 2004). VADM estimates derived from atmospheric ^{14}C (Muscheler et al., 2005) are not consistent with estimates from ^{36}Cl and ^{10}Be from Greenland ice, particularly for 10-30 ka (Fig. 1b). Discrepancies may be due to differing transport pathways for ^{36}Cl and ^{10}Be from the atmosphere to ice, diffusion of ^{36}Cl in firn (not likely in Greenland), and changes in the carbon cycle, particularly changes in ocean ventilation (e.g. Skinner and Shackleton, 2004; Muscheler et al., 2004; Robinson et al., 2005; Skinner et al., 2010; Chen et al., 2015). Furthermore, revisions in ice-core timescales directly impact the radionuclide flux calculation. For the last glacial maximum (LGM) interval, the latest Greenland ice core timescale (Svensson et al., 2008) results in adjustments to the ^{10}Be-based VADM estimates of Muscheler et al. (2005).

Magnetic concentration parameters in sediments, such as susceptibility or anhysteretic remanent magnetization (ARM) intensity, are less affected by subtle drilling

94 disturbance than natural remanent magnetization (NRM) intensities. Sedimentary NRM
95 intensities depend on magnetic grain alignment, and are an essential entity in RPI
96 proxies. Published RPI stacks (Fig. 1a) rely largely on cores collected from the *Marion*
97 *Dufresne* (MD) using the Calypso corer, and cores collected using the Advanced Piston
98 Corer (APC) of the Ocean Drilling Program and Integrated Ocean Drilling Program
99 (ODP/IODP). The stretching (oversampling) of the upper part of sediment cores collected
100 by the Calypso corer has been well documented (Skinner and McCave, 2003; Széréméta
101 et al., 2004). Deformation of the upper part of APC cores is less well documented
102 although familiar to shipboard scientists who regularly observe poorly consolidated or
103 "soupy" conditions in the topmost few meters of recovered sediment. Drilling disturbance
104 of APC cores down-section has been associated with shearing of the sediment as the APC
105 core-barrel rips through the sediment and physically deflects the ancient magnetization
106 particularly at core edges (Acton et al., 2002). This secondary magnetization component
107 tends to have a coercivity spectrum that overlaps with the ancient (primary)
108 magnetization, being largely produced by magnetic grain deflection, and therefore the
109 primary magnetization is often not recoverable through laboratory demagnetization
110 (Acton et al., 2002).
111 The influence of drilling disturbance can be mitigated to some extent by choosing
112 sites with elevated mean sedimentation rates, so that the uppermost few meters of the
113 sediment sequence have a more restricted (younger) age range, and by choice of coring
114 and sampling methods. With these factors in mind, we investigated the RPI record for the
115 latest Quaternary (0-45 ka) from a suite of short (NIOZ-type) piston cores and Kasten
116 cores (Zangger and McCave, 1990) collected from the SW Iberian Margin during cruise
117 JC089 of the RSS *James Cook* in August 2013 (Hodell et al., 2014). The coring methods
118 used during JC089 are not immune to drilling disturbance; however, traditional piston
119 cores and especially square barrel Kasten cores are expected to be less susceptible to
120 drilling disturbance than Calypso or APC cores (Skinner and McCave, 2003). The JC089
121 sites are located on a spur on the continental slope of the Iberian Margin (Promonotorio
122 dos Principes de Avis) that is elevated above the abyssal plain and the influence of
123 turbidites (Fig. 2). Uppermost Quaternary sediments comprise greenish-gray hemipelagic
124 nannofossil mud and clays with mean sedimentation rates in the 10-20 cm/kyr range

(Table 1). Our discussion includes JC089 cores collected from water depths >2500 m (Table 1); cores collected at shallower water depth during the same cruise display more significant heterogeneity in both lithology and magnetic properties.

The site locations are in the vicinity of Core MD95-2042 (Fig. 2) made famous by Shackleton et al. (2000, 2004) due to their observation that planktic and benthic $\delta^{18}O$ records mimic Greenland and Antarctic ice-core air-temperature records, respectively. As a result, sediment cores from this part of the Iberian Margin have potential for precise age control over the last glacial cycle through correlation to ice-core chronologies. One of the sites discussed here (Station 6, Table 1) is at the same location as Core MD01-2444 (Fig. 2), and is close to (1.8 km from) IODP Site U1385. At MD01-2444 and Site U1385, precise age models have been constructed by correlation of oxygen isotope and X-ray fluorescence (XRF) core-scanning data to Core MD99-2334K and ice-core chronologies (Skinner et al., 2003; Skinner and Shackleton, 2004; Hodell et al., 2013, 2015; Freeman et al., 2016). The SW Iberian Margin has distinct chronological advantages relative to most marine sites where traditional oxygen isotope stratigraphy usually has limited resolution, even at glacial terminations, resulting in poor stratigraphic control within the last glacial cycle. Core MD95-2042 was one of several cores used to build the Portuguese Margin RPI stack (Thouveny et al., 2004) that was accompanied by sedimentary $^{10}Be/^{9}Be$ data (Carcaillet et al., 2004; Ménabréaz et al., 2011). Although magnetite dominates the magnetic properties of Cores MD95-2042 and MD01-2444, the suitability of these sediments for RPI studies is compromised by the presence of a high-coercivity magnetic phase (Moreno et al., 2002), believed to be hematite sourced from eolian dust, or possibly from riverine input (Channell et al., 2013; Hodell et al., 2013).

2. XRF methods and age control

The JC089 cores were scanned at the University of Cambridge using an Avaatech XRF core scanner (3rd generation) to obtain semi-quantitative elemental data. The surface of the cores was scraped clean then covered with 4 µm thick SPEXCertiPrep Ultralene foil to avoid contamination and to prevent the cores drying out and cracking. Each section was measured at three different voltages and currents: 10 kV and 750 mA, 30 kV and 500 mA, and at 50 kV and 1000 mA. The entire length of each core was analyzed at

5-mm resolution with an irradiated surface length and width of 5 mm (downcore) and 12 mm (cross core). The count time was 60 s for each measurement. Element intensities were obtained by post-processing of the XRF spectra using the Canberra WinAxil software with standard software settings and spectrum-fit models.

Sediments deposited on the SW Iberian Margin were particularly responsive to Quaternary climate on both millennial and orbital timescales, being optimally positioned to respond to fluctuations in sea-surface and bottom-water temperatures (Shackleton et al., 2000, 2004; Skinner et al., 2003, 2007; Hodell et al., 2013, 2015). Variations in carbonate concentrations in sediments from this region have been associated with changes in terrigenous supply (Thomson et al., 1999, 2000), although surface-water productivity and sea-surface temperatures affect carbonate content on millennial timescales (Hodell et al., 2013). For Core MD01-2444, same location as JC089-06 (Fig. 2), the Ca/Ti ratio from XRF core-scanning provides a reliable proxy for wt % $CaCO_3$, and largely reflects the mixing ratio of biogenic (Ca) and detrital (Ti) components (Hodell et al., 2013). The Ca/Ti ratio at MD01-2444 mimics planktic $\delta^{18}O$ and can be correlated to the Greenland ice-core $\delta^{18}O$ record for the last glacial cycle (Hodell et al., 2013).

For this study, age models for JC089 cores were constructed by correlating Ca/Ti and Zr/Sr signals to the L* reflectance record from Cariaco Basin (Deplazes et al., 2013). The Cariaco age model is a hybrid of layer counting, radiocarbon, and correlation of the L* record to the ice core $\delta^{18}O$ record of NGRIP using the GICC05 age scale for 0-60 ka (see supplement of Deplazes et al., 2013). Peaks in Ca/Ti mark interstadials whereas Zr/Sr values are generally higher during stadials, particularly Heinrich stadials (Fig. 3; Figs. S1-S4). We used the Cariaco Basin record as the intermediary to Greenland because Heinrich stadials are well expressed in the Cariaco color record, whereas they are muted in the Greenland ice core $\delta^{18}O$ and dust record. There are only very minor differences between our age models constructed via Cariaco and those of Freeman et al. (2016) in which the same JC089 cores were correlated directly to Greenland (Figs. S5 and S6).

Precise age control from correlation to ice-core chronologies is a result of heterogeneity in geochemistry and lithology as a result of the high fidelity response of these sediments to climatic change. The heterogeneity that facilitates the age control is,

187 on the other hand, not advantageous for relative paleointensity determinations that rely on
188 uniformity in magnetic properties.
189
190 3. Magnetic measurements and methods
191 Magnetic measurements using a 2G Enterprises pass-through cryogenic
192 magnetometer (Weeks et al., 1993) were made on u-channel samples (2 x 2 x 150 cm^3)
193 collected from the split face of piston cores and the scraped side of Kasten cores.
194 Cleaning/scraping of the surfaces prior to u-channel sampling is particularly critical for
195 Kasten cores because of the likelihood of coring disturbance close to core-walls and
196 hence close to the u-channel sample. NRM was measured prior to alternating field (AF)
197 demagnetization and after demagnetization at peak fields of 10-30 mT in 5mT steps, 30-
198 60 mT in 2.5 mT steps and 60-70 mT in 5 mT steps, and 80 mT. All magnetometer
199 measurements were carried out at 1-cm spacing, with a 10-cm leader and trailer at the
200 ends of the u-channel sample. NRM component magnetizations were determined in a
201 uniform 20-80 mT demagnetization range, and maximum angular deviation (MAD)
202 values were determined using the standard method (Kirschvink, 1980) and the software
203 of Xuan and Channell (2009). Volume magnetic susceptibility was then measured at 1-
204 cm spacing using a susceptibility track designed for u-channel samples (Thomas et al.,
205 2003). ARM was then imposed along the long-axis of u-channel samples using a 50 μT
206 DC field and a 100 mT alternating field. The ARM was then AF demagnetized at peak
207 fields of 10-60 mT in 5 mT steps, and 60-80 mT in 10 mT steps. ARM was then
208 incrementally imposed along the axis of each u-channel sample using a uniform (50 μT)
209 DC field and stepwise increasing alternating fields, using the same AF increments as for
210 ARM demagnetization. Next, an isothermal remanent magnetization (IRM) was imposed
211 along the axis of each u-channel using a DC field of 300 mT, and the $IRM_{0.3T}$ was then
212 demagnetized at the same peak field used for ARM demagnetization. Finally, an IRM_{1T}
213 was imposed using a DC field of 1 T, and again demagnetized using the same alternating
214 fields used for ARM and $IRM_{0.3T}$.
215 Relative paleointensity (RPI) proxies in sediments are determined by
216 normalization of NRM intensity by the intensity of a laboratory-induced magnetization
217 designed to activate the same magnetic grains that contribute to the NRM (Levi and

Banerjee, 1976; Tauxe, 1993). The most commonly used normalizers are ARM and IRM. The NRM and the normalizer should be carried by magnetite in a restricted grain size and concentration range (see Tauxe, 1993). Here we acquire potential paleointensity proxies for the 20-60 mT demagnetization/acquisition interval using four slopes: NRM demagnetization versus ARM demagnetization, NRM demagnetization versus ARM acquisition, NRM demagnetization versus $IRM_{0.3T}$ demagnetization, and NRM demagnetization versus IRM_{1T} demagnetization. The software of Xuan and Channell (2009) allows linear correlation coefficients (r) to be determined for slopes determined at each 1-cm spaced measurement position.

A Princeton Measurements Corp. vibrating sample magnetometer (VSM) was used to determine hysteresis ratios and first order reversal curves (FORCs) on sediment samples encased in #4 gel-caps. No FORCs are reproduced in this paper as the FORC results and conclusions are very similar to those for Core MD01-2444 (Channell et al., 2013).

4. Magnetic properties

NRM has low coercivity in Core MD01-2444 (Channell et al., 2013) and at neighboring sites including MD95-2042 (Thouveny et al., 2004). The magnetic properties of Core MD01-2444 are dominated by biogenic and detrital magnetite with a greater proportion of biogenic magnetite in interglacial stages (Channell et al., 2013). Fine-grained hematite in Core MD01-2444 is indicated by S-ratios and a* (570-560 nm) reflectance data, and it was associated with eolian Saharan dust due to precessional power in a* reflectance data (Hodell et al., 2013; Channell et al., 2013). In JC089 cores, the NRM component directions have low coercivity, are associated with low (<5°) MAD values, and inclinations are consistent with site latitude although with shallower inclinations at depth (Fig. 4) possibly associated with sediment compaction. The characteristic (primary) NRM magnetization components are not obviously correlated amongst the cores, and the Laschamp or Mono Lake magnetic excursions are not observed in any of the JC089 cores, or in Core MD01-2444, although the Laschamp excursion is apparently represented by divergent declinations for several adjacent u-channel measurement positions in Core MD95-2042 (Thouveny et al., 2004). Recordings

of directional aberrations associated with Laschamp and Mono Lake excursions are rare in sediments with similar (~15 cm/kyr) sedimentation rates, presumably due to filtering of the directional signal by non-instantaneous remanence-acquisition, the stochastic nature of sediment accumulation on short timescales, and the centennial-scale duration of these two directional excursions (see Laj and Channell, 2015).

Orthogonal projections of u-channel AF demagnetization data of JC089 Kasten cores (Fig. 5a) are displayed at sediment depths of 100 cm, 200 cm, 250 cm, and ~350 cm (300 cm corresponds to a section break). For one core (06-5K), the projection at 330 cm is shown because the core does not reach 350 cm (Table 1). A single NRM magnetization component appears to be present throughout the suite of cores, and the maximum peak field (80 mT) implies low coercivity NRM carrier(s). Orthogonal projections from samples at these depths in JC089 piston cores are shown in Figure S7.

Volume susceptibility shows subdued variability other than during HS4 (Fig. 6d) Variations in the magnetite grain-size parameter κ_{arm}/κ indicate coarser magnetite during Heinrich stadials (HS), a progressive fining of grain size at Termination I, and fine magnetite grain sizes in the early Holocene (Fig. 6c). The change in κ_{ARM}/κ at Termination I is controlled by an increase, by a factor of ~2, of ARM intensity as the concentration of fine-grained biogenic magnetite increases relative to coarser detrital magnetite in the Holocene. The plot of κ_{arm} versus susceptibility (κ) indicates fine magnetite grain sizes apart from during HS4 (Fig. 6a), and the range of magnetite grain sizes is consistent with estimates from the hysteresis (Day et al., 1977) plot (Fig. 6b). Our interpretation of the magnetic properties of JC089 cores is consistent with the interpretations from Core MD01-2444 where magnetic properties are controlled by variations in the proportion of biogenic and detrital magnetite (Channell et al., 2013) with interglacial stages, including the Holocene, characterized by enhanced concentration of biogenic magnetite, whereas Heinrich stadials have enhanced detrital input associated with sea level low-stands. High susceptibility and coarse magnetite grain size during HS4 (Fig. 6) are consistent with the presence of ice-rafted debris (IRD). Heinrich stadials tend to be associated with lower values of κ_{arm}/κ (coarser magnetite grain size), higher susceptibility and higher S-ratios, but only HS4 has the prominent susceptibility signal denoting IRD (Fig. 6).

In Cores MD95-2042 and MD□□□□□□□□□□□□□□□□□□ magnetic mineral was detected by Moreno et al. (2002) and Channell et al. (2013), respectively, and attributed to eolian dust (Hodell et al., 2013). In Core MD01-2444, isothermal remanent magnetization acquired in magnetizing fields of 300 mT ($IRM_{0.3T}$) and 1 T (IRM_{1T}) yield S-ratios (determined as $IRM_{0.3T}$ / IRM_{1T} after demagnetization of both IRMs at peak fields of 30 mT) with values in the 0.8-0.95 range with lower values (high coercivities) associated with glacial and stadial climatic episodes (see Fig. 5 in Channell et al., 2013). For JC089 cores, the values of $IRM_{0.3T}$ and IRM_{1T} yield S-ratios in a similar (0.8-0.95) range although values are variable from core to core (Fig. 6e). Using two of the sediment depths (100 cm and 200 cm) used for orthogonal projections of NRM (Fig. 5a), normalized intensities (Jr/Jo) of NRM indicate higher coercivity in the 20-80 mT peak field demagnetization range than for ARM (Fig. 5b). Both $IRM_{0.3T}$ and IRM_{1T} have higher coercivity in the 60-80 mT range than NRM and ARM (Fig. 5b). The progressive bifurcation with increasing peak fields for $IRM_{0.3T}$ and IRM_{1T} denotes the high-coercivity signal of the hematitic dust that is apparently less important in NRM and ARM (Fig. 5b).

5. Relative paleointensity (RPI) proxies

RPI proxies in these sediments are complicated by the presence of biogenic magnetite (see Roberts et al., 2012), and by the presence of detrital hematite, as RPI proxies traditionally require magnetite to be the sole remanence carrier with uniformity in magnetite grain size and concentration (Tauxe, 1993). On the other hand, the hematite in Core MD01-2444 is from eolian dust, or possibly from riverine input, and therefore detrital (Hodell et al., 2013), and therefore may not contribute to the NRM due to the low intrinsic magnetization (alignment efficiency) of hematite. The possibility of acquiring useful RPI proxies depends on the extent to which the detrital hematite contributes to the NRM and to the normalizers used to acquire the RPI proxies.

Core MD01-2444 and Cores 06-4K and 06-5K were collected at the same location (Fig. 2), and yet the MD01-2444 apparent sedimentation rates are about twice those at 06-4K and 06-5K (Fig. 7), presumably because of relative stretching of the MD core. The two Kasten cores (06-4K and 06-5K) have similar but not identical sedimentation rates

311 with differences attributable to differential compaction (Figs. S5 and S6). Clearly, cores
312 collected at nominally the same location are not identical, and depend on the coring
313 method, and perhaps on the precise location of core penetration. RPI proxies from the
314 three cores differ, particularly in the 12-15 ka interval (Fig. 7). The Ca/Ti and Zr/Sr ratios
315 for 06-4K (Fig. 3; Figs. S2 and S4) imply a hiatus that apparently removed part or all of
316 the Younger Dryas, which appears to be recorded in 06-5K (Fig. 3). Note that all four
317 RPI proxies (NRM/ARM, NRM/ARMAQ, NRM/$IRM_{0.3T}$, NRM/IRM_{1T}) are similar in
318 the glacial interval, but differ in the Holocene, although correlation coefficients (r)
319 associated with all slopes are close to unity, implying well-defined slopes (Fig. 7). A
320 similar difference in the four RPI proxies was observed in the Holocene at MD01-2444
321 and was attributed to under-normalization by IRM due to high concentration of ultra-fine
322 biogenic magnetite (Channell et al., 2013). A fine-grained high-coercivity hematitic
323 phase would be expected to affect the four proxies differently, and the general similarity
324 of the RPI proxies implies that the hematite does not contribute significantly to NRM
325 intensity or to the normalizers used to generate the RPI proxies.
326 For other JC089 cores (Table 1), linear sedimentation rates are not identical for
327 Kasten and piston cores from the same location, attributable to differential coring
328 disturbance, with the piston cores having generally higher linear sedimentation rates (Fig.
329 8; Figs. S5 and S6). The four RPI proxies (NRM/ARM, NRM/ARMAQ, NRM/$IRM_{0.3T}$,
330 NRM/IRM_{1T}) are generally similar although again there is the tendency, as in Cores 06-
331 4K and 06-5K (Fig. 7), for under-normalization by IRM in the Holocene where the
332 concentration of ultra-fine biogenic magnetite is greater (Fig. 8). The linear correlation
333 coefficients (r) are generally >0.98, indicating that the slopes (RPI proxies) are well
334 defined. Note that all RPI proxies (slopes) were determined for the 20-60 mT
335 demagnetization/acquisition range in an effort to exclude the enhanced influence of
336 hematite at peak fields >60 mT (Fig. 5b).
337
338 6. Relative paleointensity (RPI) stacks
339 In order to test the fidelity of the RPI proxies, we constructed a RPI stack for the
340 SW Iberian Margin for the 0-45 ka interval for comparison with other records. The
341 Iberian Margin Stack (Fig. 9a) includes the ten JC089 cores (Table 1, Fig. 9b), the RPI

record from Core MD01-2444 (Table 2, Channell et al., 2013) and the Portuguese Margin Stack (Table 2, Thouveny et al., 2004). All records are on their individual age models, with no age adjustments or record matching. The JC089 and MD01-2444 RPI proxies that are incorporated in the stack are the slopes of NRM/ARM. Each record was interpolated to a uniform 0.5-kyr sampling spacing, and set to a common mean and common standard deviation. The stack is the mean at each 0.5-kyr data step, giving equal weight to each of 12 records (Fig. 9a).

The choice of records for inclusion in the stack from outside the Iberian Margin for 0-45 ka (Table 2) was based on mean sedimentation rate (>15 cm/kyr) and deemed adequacy of age models. The vast majority of marine cores do not have adequate sedimentation rates, nor do they have age control in the last glacial other than identification from $\delta^{18}O$ of the last glacial termination. The twelve records that are included in the stack from outside the Iberian Margin (Fig. 9c) are listed in Table 2. Each record was placed on its published age model, was interpolated to a uniform 0.5-kyr sampling spacing, and set to a common mean and common standard deviation. The stack is the arithmetic mean at each 0.5-kyr data step (Fig. 9a).

The lacustrine records included in the 0-45 ka stack from outside the Iberian Margin (Table 2) are the Lac du Bouchet (France) record of Thouveny et al. (1993), the Lake Biwa (Japan) record of Hayashida et al (2007), the Lake Potrok Aike (Patagonia) record of Lisé-Pronovost et al. (2013), the Lake Van (Turkey) record of Vigliotti et al. (2014), and the Lake Towuti (Indonesia) record of Kirana et al. (2018). Lisé-Pronovost et al. (2013) offered a "corrected" NRM/ARM RPI proxy record, designed to compensate for the influence on RPI of magnetic grain-size changes. The correction method was originally applied to NRM/IRM data from Lake Pepin (Brachfeld and Banerjee, 2000), and has rarely been used since. We utilize the Potrok Aike RPI record before "correction" because we have concerns about the veracity of the correction, particularly for NRM/ARM data. Age models for lacustrine RPI data incorporated in the stack are as published, and are based on radiocarbon, tephrochronology, and for Lake Van, correlation of XRF core-scanning records to ice-core chronologies.

The marine RPI records included in the 0-45 ka stack from outside the Iberian Margin (Table 2) are the Black Sea record of Nowaczyk et al. (2013), the Rockall Trough

record of Channell et al. (2016), the ODP Site 1063 record of Channell et al. (2012), the Bermuda Rise record of Schwartz et al. (1996), the Philippine Sea record of Stott et al. (2002), the ODP Site 1089 (South Atlantic) record of Stoner et al. (2003), and the Scotia Sea record of Xiao et al. (2016). Age models are as published apart from the ODP Site 1063 age model where a single additional age-depth point has been added to the published age model (Channell et al., 2012). Age models are based on combinations of orbitally-tuned oxygen isotope data, radiocarbon, tephrochronology and correlation to ice-core chronologies.

For the stack from outside the Iberian Margin, the 12 records were interpolated to a uniform 0.5-kyr sampling spacing, and set to a common mean and common standard deviation. The stack is the mean at each 0.5-kyr time-step, giving equal weight to each of the twelve records (Fig. 9a).

Finally an overall stack (Fig. 9a) was constructed by combining the individual records from outside the Iberian Margin with a stack of all 10 JC089 records, the Portuguese Margin Stack of Thouveny et al. (2004) and the MD01-2444 record of Channell et al. (2013), giving equal weight to each record. Again, all records are on their individual (published) age models, with no age adjustments (apart from a single extra age tie-point for Site 1063) or record matching.

7. Discussion

Individual RPI records in the SW Iberian Margin stack (Fig. 9b) and in the stack from outside the Iberian Margin (Fig. 9c) show considerable variability. Age model discrepancies account for some of this variability, and the saw-tooth character of some of individual records reflects low resolution at the 0.5 kyr sampling step. Rather than emphasizing individual higher resolution records, we assign equal weight to each record in the two stacks, and construct an overall stack as described above, that comprises a combination of three Iberian Margin records and 12 records from outside the Iberian Margin. The resulting stacks are similar to one another (Fig. 9a), but are very different from the published stacks for this time interval (Fig. 1a). The Holocene part of the RPI stacks can be only broadly matched to the Holocene compilations, CALS10k.1b and SHA.DIF.14k of Korte et al. (2011) and Pavon-Carrasco et al. (2014) (Fig. 9a). The

scaling of the stacks to VADM was accomplished by matching the stacks to CALS10k.1b and SHA.DIF.14k and assuming a VADM of ~3 x10^{22} Am^2 for the Laschamp RPI minimum (Fig. 9a). The pre-Holocene part of the RPI stacks are characterized by a RPI shoulder (notch) at ~13-14 ka, that is represented in some individual records by a RPI minima (Figs. 9 b,c), and is preceded by a RPI high at ~15-18 ka (Fig. 9a). The decrease in RPI from ~20 ka to the Laschamp excursion at ~41 ka is marked by two poorly defined minima at ~26-30 ka and 34 ka. These RPI minima occur in some individual records, and are smoothed by the stacking process. In one of the cores included in the stack from outside the Iberian Margin (Core MD04-2822 from Rockall Trough), a directional excursion was recorded within a RPI minimum at 26.5 ka (Channell et al., 2016).

Previously published estimates of geomagnetic field intensity (VADM) since 30 ka from Greenland ^{36}Cl and ^{10}Be records, and from estimated atmospheric ^{14}C concentrations (Muscheler et al., 2005) do not resemble one another (Fig. 1b) or previously published RPI stacks (Fig. 1a), or the stacks resolved here (Fig. 9a). The resemblance amongst the previously published cosmogenic-based estimates of VADM is improved prior to 30 ka (Fig. 1b), possibly because cosmogenic isotope production is more sensitive to low field intensity, and is relatively insensitive to field intensities higher than modern (Masarik and Beer, 2009).

The peak in RPI stacks at 15-18 ka (Fig. 9a) may partially explain the well-documented drop in atmospheric $\Delta^{14}C$ in the "mystery interval" at 17.5-14.5 kyr (Broecker and Barker, 2007). The apparent lag of a peak in RPI at ~15-18 ka relative to the peak VADM at 14.5 ka inferred from ^{14}C production (Fig. 10) may be attributable to lock-in delay in acquisition of the remanent magnetization, with a ~2 kyr lag at a 10-15 cm/kyr sedimentation rate being equivalent to ~20-30 cm lock-in depth. On the other hand, no such offset is observed at the Laschamp excursion where ages from lavas and sediments agree rather well (e.g., Laj et al., 2014). Immediately after the RPI high at ~15-18 ka, a RPI minimum at ~13.5 ka is observed in some individual records (Fig. 9), notably in Core MD01-2444 where it is accompanied by a directional magnetic excursion (Channell et al., 2013). This excursion has not been observed elsewhere, and it is not present in any of the JC089 cores, although an excursion of similar age from $^{40}Ar/^{39}Ar$

methods (at ~17 ka) has been documented in the Tianchi Volcanics in China (Singer et al., 2014).

The new overall VADM stack from Figure 9a, combined with the CALS10k.1b model for the Holocene (Korte et al., 2011), is now compared with updated calculations of VADM from Intcal13 atmospheric ^{14}C (Reimer et al., 2013) and Greenland ^{10}Be using a current Greenland ice core timescale (Svensson et al., 2008). The updated VADM calculation based on ^{10}Be (Fig. 10a), using recent ^{10}Be production models (Poluianov et al., 2016; Herbst et al., 2017), is different from those shown in Figure 1b (from Muscheler at al., 2005) since the timescale update results in corresponding revisions in accumulation rates and ^{10}Be flux. Here we based the ^{10}Be flux calculation on the average GRIP and GISP2 ^{10}Be record (Muscheler at al., 2005) and adjusted the accumulation rate and ^{10}Be flux to be consistent with the most recent Greenland ice core timescale (Svensson et al., 2008). This procedure may lead to a significant climate signal in the ^{10}Be flux (e.g., Adolphi et al., 2014), however; it is not clear how such potential climate influence can be identified and corrected over longer timescales. The new calculations indicate that although the ^{10}Be-based VADM fits rather well with the overall VADM stack, the ^{14}C-based VADM does not (Fig. 10), presumably due to changes in carbon cycling over the last Termination and probably also due to an underestimated ^{14}C production rate. Nevertheless, the overall VADM stack can explain the atmospheric ^{14}C trend from about 25 to 15 ka as indicated by the similar trends in the VADM stack and ^{14}C-based geomagnetic field during this period (Fig. 10).

8. Conclusions

Based on 24 sedimentary RPI records from the SW Iberian Margin and elsewhere (Tables 1 and 2), we make the case for a revised view of geomagnetic field intensity in the latest Pleistocene (10-30 ka). We construct a stack of RPI data from 10 sediment cores recovered during Cruise JC089 (Table 1). This stack is combined with two previously published records from the Iberian Margin (Thouveny et al., 2004; Channell et al., 2013) and with 12 RPI records from outside the Iberian margin (Table 2) to produce an overall RPI stack (Fig. 9a). The RPI stacks feature a high in RPI at ~15-18 ka that is followed by a shoulder (notch) at 13-15 ka as RPI decreases to a minimum at ~9 ka. In

some individual records (Fig. 9), the notch at 13-15 ka is manifest as a low in RPI that is largely smoothed out by stacking. In one record, MD01-2444 (Table 2), a RPI low at 13.5 ka is associated with a directional magnetic excursion (Channell et al., 2013).

The overall stack indicates a progressive increase in RPI from the low in RPI at ~41 ka associated with the Laschamp magnetic excursion to a high at 15-18 ka corresponding to late HS1 (Fig. 10). A low in RPI at ~34 ka, associated with the Mono Lake magnetic excursion, and at ~26-30 ka are manifest by more pronounced RPI minima in some individual records. A prominent RPI minimum at 26.5 ka is accompanied by a directional excursion in the Rockall Trough record (Table 2, Channell et al., 2016).

The inconsistent picture of RPI in the 10-30 ka interval from published RPI stacks (Fig. 1a) is attributed to poor preservation of recovered sediment in the uppermost part of sediment sequences, particularly those recovered by Calypso cores and the APC used by ODP/IODP. The cores incorporated into our stacks are not immune to drilling disturbance, but we minimize disturbance by preferentially selecting cores recovered using conventional piston and Kasten (gravity) coring, and cores with mean sedimentation rates >15 cm/kyr.

The new overall RPI stack is supported by a revised calculation of VADM from Greenland ^{10}Be flux (Fig. 10) using a recent ice-core timescale (Svensson et al., 2008) although a possible climate influence on the ^{10}Be flux is hard to assess. The overall RPI stack is, on the other hand, inconsistent with the estimated VADM from atmospheric ^{14}C (Fig. 10). The new overall RPI stack, even with 2 kyr magnetization lock-in delay, cannot explain atmospheric ^{14}C levels (Reimer et al., 2013), not only during the "Mystery Interval" but also back to 45 ka although it can explain the atmospheric ^{14}C trend from ~25 to 15 ka (Fig. 11). An increase in marine radiocarbon ventilation in late HS1 and/or the onset of the Bølling-Allerød has been observed in numerous records (e.g. Skinner and Shackleton, 2004; Robinson et al., 2005; Skinner et al., 2010, 2014, 2015; Burke and Robinson, 2012; Chen et al., 2015; de la Fuente et al., 2015; Umling and Thunell, 2017). If the timing of the observed RPI maximum is accurate, at ~15-18 ka (Fig. 10), this would raise the bar for the magnitude of marine radiocarbon ventilation change that would be needed to fully account for the atmospheric Δ^{14}C record, as it would imply an

increasing trend in radiocarbon production while atmospheric radiocarbon activity was decreasing. Offsets between observed atmospheric $\Delta^{14}C$ changes and modeled atmospheric $\Delta^{14}C$ changes (e.g. derived from ^{10}Be- or RPI-based reconstructions of variable radiocarbon production rates, using an ocean outcrop-diffusion box-model), can provide an indication of how much atmospheric $\Delta^{14}C$ variability might be attributed to carbon cycle changes rather than ^{14}C production rate changes (Figure 11a). Across the deglaciation, these offsets track atmospheric CO_2 closely (Figure 11c), and share many features with available marine radiocarbon ventilation records, suggesting an ocean ventilation influence on atmospheric $\Delta^{14}C$ and CO_2. However, it is also notable that the existing marine radiocarbon ventilation records exhibit smaller changes than would seem to be required to fully reconcile the observed atmospheric $\Delta^{14}C$ record and the revised ^{10}Be and RPI records (Figure 11b). Therefore, while several independent records strongly support the combined influence of ocean ventilation and ^{14}C production changes on atmospheric $\Delta^{14}C$ and CO_2 during the last ice age and over the last Termination, a complete solution to the mystery of deglacial radiocarbon and carbon cycling remains elusive.

Acknowledgments

The overall RPI stack, scaled to VADM, is in Table S1. The ^{10}Be-based estimate of geomagnetic field intensity is in Table S2. This work was made possible by NERC support (NE/J00653X/1) for Cruise 089 aboard the RSS *James Cook* that permitted collection of the cores for this study. JETC acknowledges support from US NSF grants EAR-1014506 and OCE-0850413, LCS from UK NERC grant NE/L006421/1, and RM from Swedish Research Council grant DNR2013-8421. We thank Kainian Huang for laboratory assistance, Nicolas Thouveny, Agathe Lisé-Pronovost, Wenshen Xiao and Kartika Kirana for sending requested data, and Claude Hillaire-Marcel for editorial guidance.

References

Acton, G.D., M. Okado, B.M. Clement, S.P. Lund and T. Williams, Paleomagnetic overprints in ocean sediment cores and their relationship to shear deformation caused by piston coring. J. Geophys. Res., 107, B4, 2067, 10.1029/2001JB000518, 2002.

Adolphi, F., R. Muscheler, A. Svensson, A. Aldahan, G. Possnert, J. Beer, J. Sjolte, S. Bjorck, K. Matthes and R. Thiéblemont, Persistent link between solar activity and Greenland climate during the Last Glacial Maximum. Nature Geoscience 7, 662-666, 2014.

Bard, E., F. Rostek, and G. Menot-Combes, Radiocarbon calibration beyond 20,000 ^{14}C yr B.P. by means of planktonic foraminifera of the Iberian Margin. Quaternary Research, 61, 204– 214, 2004.

Baumgartner, S., J. Beer, J. Masarik, G. Wagner, L. Meynadier, H.-A. Synal, Geomagnetic modulation of the ^{36}Cl flux in the GRIP ice core, Greenland. Science 279,1330–1332, 1998.

Beck, J.W., D.A. Richards, R.L. Edwards, B.W. Silverman, P.L. Smart, D.J. Donahue, S. Hererra-Osterheld, G.S. Burr, L. Calsoyas, A.J.T. Jull, D. Biddulph, Extremely large variations of atmospheric 14C concentration during the last glacial period, Science 292, 2453–2458, 2001.

Brachfeld, S., and S.K. Banerjee, A new high-resolution geomagnetic paleointensity record for the North American Holocene: a comparison of sedimentary and absolute intensity data. J. Geophys. Res. 105 (B1), 821-834, 2000.

Broecker, W. and S. Barker, A 190‰ drop in atmospheric $\Delta^{14}C$ during the "Mystery Interval" (17.5-14.5 kyr). Earth Planet Sci. Letters, 256, 90-99, 2007.

Bronk Ramsey, C., et al., A complete terrestrial radiocarbon record for 11.2 to 52.8 kyr B.P., Science 338, 370, 2012.

Burke, A. and L.F. Robinson, The Southern Ocean's role in carbon exchange during the last deglaciation. Science 335, 557-561, 2012.

Carcaillet, J.T., D. L. Bourles, N. Thouveny and M. Arnold, A high resolution authigenic 10Be/9Be record of geomagnetic moment variations over the last 300 ka from sedimentary cores of the Portuguese margin. Earth and Planetary Science Letters 219 (2004) 397-412, 2004.

Carter-Stiglitz, B., B. Moskowitz and M. Jackson, Unmixing magnetic assemblages and the magnetic behavior of bimodal mixtures. J. Geophys. Res., 106, 26,397-26, 411, 2001.

Channell, J.E.T., Xuan, C. and Hodell, D.A., Stacking paleointensity and oxygen isotope data for the last 1.5 Myrs (PISO-1500). Earth Planet. Sci. Letters, 283, 14-23, 2009.

Channell, J.E.T., D.A. Hodell and J.H. Curtis, ODP Site 1063 (Bermuda Rise) revisited: oxygen isotopes, excursions and paleointensity in the Brunhes Chron. Geochem. Geophys. Geosyst. (G^3), 13(1), Q02001, doi:10.1029/2011GC003897, 27 pp., 2012.

Channell, J.E.T., D.A. Hodell, V. Margari, L.C. Skinner, P.C. Tzedakis, and M.S. Kesler, Biogenic magnetite, detrital hematite, and relative paleointensity in sediments from the Southwest Iberian Margin, Earth Planet. Sci. Letters, 376, 99-109, 2013.

Channell, J. E. T., R. J. Harrison, I. Lascu, I. N. McCave, F. D. Hibbert, and W. E. N. Austin, Magnetic record of deglaciation using FORC-PCA, sortable-silt grain size, and magnetic excursion at 26 ka, from the Rockall Trough (NE Atlantic), Geochem.

569 Geophys. Geosyst., 17, 1823–1841, doi:10.1002/2016GC006300, 2016.
570 Chen, T., L.F. Robinson, A. Burke, J. Southon, P. Spooner, P.J. Morris and H.C. Ng,
571 Synchronous centennial abrupt events in the ocean and atmosphere during the last
572 deglaciation. Science 349, 1537-1541, 2015.
573 Day, R., M. Fuller, and V.A. Schmidt, Hysteresis properties of titanomagnetites: grain-
574 size and compositional dependence. Phys. Earth Planet. Int., 13, 260-267, 1977.
575 Deplazes, G., A. Lückge, L.C. Peterson, A. Timmermann, Y. Hamann, K.A. Hughen, U.
576 Röhl, C. Laj, M.A. Cane, D.M. Sigman, and G.H. Haug, Links between tropical
577 rainfall and North Atlantic climate during the last glacial period, Nature Geoscience
578 6, 213-217, 2013.
579 de la Fuente, M., L. Skinner, E. Calvo, C. Pelejero and I. Cacho, Increased reservoir ages
580 and poorly ventilated deep waters inferred in the glacial Eastern Equatorial Pacific.
581 Nat Comm., 6, 2015.
582 Dunlop, D.J., Theory and application of the Day plot (Mrs/Ms versus Hcr/Hc) 1.
583 Theoretical curves and tests using titanomagnetite data. J. Geophys. Res., 107, B3,
584 2056, doi:10.1029/2001JB000486, 2002.
585 Dunlop, D.J. and B. Carter-Stiglitz, Day plots of mixtures of superparamagnetic, single
586 domain, pseudosingle domain, and multidomain magnetites. J. Geophys. Res., 111,
587 B12S09, doi: 10.1029/2006JB004499, 2006.
588 Fairbanks, R.G., R.A. Mortlock, T.-C. Chiu, L. Cao, A. Kaplan, T.P. Guilderson, T.W.
589 Fairbanks, A.L. Bloom, P.M. Grootes, M.-J. Nadeau, Radiocarbon calibration curve
590 spanning 0 to 50,000 yr BP based on paired 230Th/234U/238U and 14C dates on
591 pristine corals, Quat. Sci. Rev. 24, 1781–1796, 2005.
592 Finkel, R.C., and K. Nishiizumi, Beryllium-10 concentrations in the Greenland ice sheet
593 project 2 ice core from 3–40 ka. J. Geophys. Res., 102, 26699–26706, 1997.
594 Freeman, E., L. C. Skinner, C. Waelbroeck, and D. A. Hodell, Radiocarbon evidence for
595 enhanced respired carbon storage in the Atlantic at the Last Glacial Maximum.
596 Nature Geoscience, 7, 11998, DOI: 10.1038/ncomms11998
597 |www.nature.com/naturecommunications, 2016.
598 Genevey, A., Y. Gallet, C. G. Constable, M. Korte, and G. Hulot, ArcheoInt: An
599 upgraded compilation of geomagnetic field intensity data for the past ten millennia
600 and its application to the recovery of the past dipole moment, Geochem. Geophys.
601 Geosyst., 9, Q04038, doi:10.1029/2007GC001881, 2008.
602 Hayashida, A., A. Mohammed, Y. Kuniko, H. Kitagawa, M. Torii and K. Takemura,
603 Environmental magnetic record and paleosecular variation data for the last 40 kyrs
604 from Lake Biwa sediments, Central Japan. Earth Planets Space, 59, 807-814, 2007.
605 Herbst, K., R. Muscheler and B. Heber, The new local interstellar spectra and their
606 influence on the production rates of the cosmogenic radionuclides ^{10}Be and ^{14}C. J.
607 Geophys. Res., Space Physics 122, 23-34, doi:10.1002/2016JA023207, 2017.
608 Hodell, D.A., Crowhurst, S., Skinner, L., Tzedakis, P.C., Margari, V., Channell, J.E.T.,
609 Kamenov, G., Maclachlan, S., and Rothwell, G., Response of Iberian Margin
610 sediments to orbital and suborbital forcing over the past 420 ka. Paleoceanography,
611 28, 1–15, doi:10.1002/palo.20017, 2013.
612 Hodell, D.A., Elderfield, H., Greaves, M., McCave, I.N., Skinner, L., Thomas, A., White,
613 N., and the JC089 Scientific Party, *JC089 Cruise Report* - IODP Site Survey of the
614 Shackleton Sites, SW Iberian Margin, British Ocean Data Centre,

https://www.bodc.ac.uk/data/information_and_inventories/cruise_inventory/report/13392/, 2014.

Hodell, D. A., L. Lourens, S. J. Crowhurst, T. Konijnendijk, R. Tjallingii, F. Jimenez-Espejo, L. C. Skinner, P. C. Tzedakis, and Members of the Shackleton Site Project, 2015. A reference time scale for Site U1385 (Shackleton Site) on the Iberian Margin, Global Planetary Change, 133: 9-64, 2015.

Hughen, K., S. Lehman, J. Southon, J. Overpeck, O. Marchal, C. Herring, J. Turnbull, ^{14}C activity and global carbon cycle changes over the past 50,000 yr. Science 303, 202–207, 2004.

King, J.W., S.K. Banerjee, and J. Marvin, A new rock-magnetic approach to selecting sediments for geomagnetic paleointensity studies: application to paleointensity for the last 4000 years. J. Geophys. Res. 88 (1983) 5911-5921, 1983.

Kirana, K.H., S. Bijaksana, J. King, G.H. Tamuntuan, J. Russell, L. O. Ngkoimani, D. Dahrin, and S.J. Fajar, A high-resolution, 60 kyr record of relative geomagnetic field intensity from Lake Towuti, Indonesia. Phys. Earth Planet. Int., 275, 9-18, 2018.

Kirschvink, J.L., The least squares lines and plane analysis of paleomagnetic data. Geophys. J.R. Astr. Soc. 62, 699-718, 1980.

Korte, M., F. Donadini, and C. Constable, Geomagnetic field for 0–3 ka: 2. Revised global time-varying models, Geochem. Geophys. Geosyst., 10, Q06008, doi:10.1029/2008GC002297, 2009.

Korte, M., C. Constable, F. Donadini, and R. Holme, Reconstructing the Holocene geomagnetic field, Earth Planet. Sci. Lett., 312, 497–505, 2011.

Laj, C., C. Kissel, A. Mazaud, J.E.T. Channell, and J. Beer, North Atlantic paleointensity stack since 75 ka (NAPIS-75) and the duration of the Laschamp event. Phil. Trans. Royal Soc. London, 358, 1009-1025, 2000.

Laj, C., C. Kissel and J. Beer, High-resolution global paleointensity stack since 75 kyr (GLOPIS-75) calibrated to absolute values. In: Timescales of the Paleomagnetic Field. J.E.T. Channell, D.V. Kent, W. Lowrie and J.G. Meert (editors), Geophysical Monograph 145, American Geophysical Union, Washington DC, 255-265, 2004.

Laj, C., H. Guillou and C. Kissel, Dynamics of the Earth's magnetic field in the 10-75 kyr period comprising the Laschamp and Mono Lake excursions: New results from the French Chaine des Puys in a global perspective. Earth Planet. Sci. Letters, 387, 184-197, 2014.

Laj, C., and J.E.T. Channell, Geomagnetic excursions. In: Treatise on Geophysics: Volume 5, Geomagnetism (editor: M. Kono). Chapter 10, 343-383, Elsevier, Amsterdam, 2015.

Lemieux-Dudon, B., E. Blayo, J.R. Petit, C. Waelbroeck, A. Svensson, C. Ritz, J.-M. Barnola, B.M. Narcisi and F. Parrenin, Consistent dating for Antarctic and Greenland ice cores. Quat. Sci. Rev. 29, 8-20, 2010.

Levi, S., and S.K. Banerjee, On the possibility of obtaining relative paleointensities from lake sediments. Earth Planet. Sci. Letters, 29, 219-226, 1976.

Lisé- Pronovost, A. G. St-Onge, C. Gogorza, T. Haberzetti, M. Preda, P. Kliem, P. Francus and B. Zolitschka, The PASADO Science Team, High-resolution paleomagnetic secular variations and relative paleointensity since the Late Pleistocene in southern South America. Quat. Sci. Rev., 71, 91-108, 2013.

660 Masarik, J. and J. Beer, Simulation of particle fluxes and cosmogenic nuclide production
661 in the Earth's atmosphere. J. Geophys. Res., 104, 12,099-12,111, 1999.
662 Masarik, J. and J. Beer, An updated simulation of particle fluxes and cosmogenic nuclide
663 production in the Earth's atmosphere. J. Geophys. Res., 114,
664 doi:10.1029/2008JD010557, 2009.
665 Ménabréaz, L., N. Thouveny, D.L. Bourles, P. Deschamps, B. Hamelin and F. Demory,
666 The laschamp geomagnetic dipole low expressed as a cosmogenic ^{10}Be atmospheric
667 overproduction at ~41 ka. Earth Planetary Science letters, 312, 305-317, 2011.
668 Monnin, E., A. Indermuhle, A. Dallenbach, J. Fluckiger, B. Stauffer, T.F. Stocker, D.
669 Raynaud and J.M. Barnola, Atmospheric CO_2 concentrations over the Last Glacial
670 Termination. Science 291, 112-114, 2001.
671 Moreno, E., N. Thouveny, D. Delanghe, I.N. McCave and N.J. Shackleton, Climatic and
672 oceanographic changes in the Northeast Atlantic reflected by magnetic properties of
673 sediments deposited on the Portuguese Margin during the last 340 ka. Earth and
674 Planetary Sci. Letters, 202, 465-480, 2002.
675 Muscheler, R., J. Beer, G. Wagner, C. Laj, C. Kissel, G. M. Raisbeck, F. Yiou, and P.W.
676 Kubik, Changes in the carbon cycle during the last deglaciation as indicated by the
677 comparison of ^{10}Be and ^{14}C records. Earth and Planet. Sci. Letters, 219, 325-340,
678 2004.
679 Muscheler, R., J. Burg, P.W. Kubik and H.A. Synal, Geomagnetic field intensity during
680 the last 60,000 years based on ^{10}Be and ^{36}Cl from the Summit ice cores and ^{14}C.
681 Quat. Sci. Revs., 24, 1849-1860, 2005.
682 Nowaczyk, N.R., U. Frank, J. Kind and H.W. Arz, A high-reolution paleointnesity stack
683 of the past 14 to 68 ka from Black Sea sediments. Earth Planet. Sci. Lett., 384, 1-16,
684 2013.
685 Pavon-Carrasco, F.J., M.L. Osete and J.M. Torta and A. De Santis, A geomagnetic field
686 model for the Holocene based on archaeomagnetic and lava flow data. Earth Planet.
687 Sci. Lett., 388, 98-109, 2014.
688 Peterson, L.C., G.H. Haug, K.A. Hughen and U. Röhl, Rapid changes in the hydrologic
689 cycle of the tropical Atlantic during the Last Glacial, Science 290, 1947–1951, 2000.
690 Poluianov, S.V., G.A. Kovaltsov, A.L. Mishev and I.G. Usoskin, Production of
691 cosmogenic isotopes 7Be, 10Be, 14C, 22Na, and 36Cl in the atmosphere: Altitudinal
692 profiles of yield functions. J. Geophys. Res. Atmos. 121, 8125–8136,
693 doi:8110.1002/2016JD025034, 2016.
694 Pressling, N., C. Laj, C. Kissel, D. Champion and D. Gubbins, Palaeomagnetic intensities
695 from ^{14}C-dated lava flows on the Big Island, Hawaii: 0-21 kyr. Earth Planet. Sci.
696 Letters, 247, 26-40, 2006.
697 Reimer, P. et al., IntCal13 and Marine13 radiocarbon age calibration curves 0–50,000
698 years cal BP. Radiocarbon 55, 4, 1869-1887, 2013.
699 Roberts, A.P., L. Chang, D. Heslop, F. Florindo and J.C. Larrasoana, Searching for single
700 domain magnetite in the "pseudo-single-domain" sedimentary haystack: Implications
701 of biogenic magnetite preservation for sediment magnetism and relative
702 paleointensity determinations. J. Geophys. Res., 117, B08104,
703 doi:10.1029/2012JB009412, 2012.

Robinson, L.F., J.F. Adkins, L.D. Keigwin, J. Southon, D.P. Fernandez, S.-L.Wang and D.S. Scheirer, Radiocarbon variability in the western North Atlantic during the last deglaciation. Science, 310, 1469-1473, 2005.

Schwartz, M., S.P. Lund and T.C. Johnson, Environmental factors as complicating influences in the recovery of quantitative geomagnetic field paleointensity estimates from sediments. Geophys. Res. Lett., 23, 2693-2696, 1996.

Shackleton, N.J., M.A. Hall, and E. Vincent, Phase relationships between millennial-scale events 64,000–24,000 years ago. Paleoceanography 15, 565–569, 2000.

Shackleton, N.J., R.G. Fairbanks, T.-C. Chiu, and F. Parrenin, Absolute calibration of the Greenland time scale: implications for Antarctic time scales and for $\Delta^{14}C$. Quat. Sci. Rev. 23, 1513-1522, 2004.

Siegenthaler, U., Uptake of excess CO_2 by an outcrop-diffusion model ocean. J. Geophys. Res., 88, 3599-3608, 1983.

Simon, Q., N. Thouveny, D. L. Bourlès, J.-P. Valet, F. Bassinot, L. Ménabréaz, V. Guillou, S. Choy, and L. Beaufort, Authigenic $^{10}Be/^{9}Be$ ratio signatures of the cosmogenic nuclide production linked to geomagnetic dipole moment variation since the Brunhes/Matuyama boundary, J. Geophys. Res. Solid Earth, 121, doi:10.1002/2016JB013335, 2016.

Singer, B. S., B. R. Jicha, H. He, and R. Zhu, Geomagnetic field excursion recorded 17 ka at Tianchi Volcano, China: New $^{40}Ar/^{39}Ar$ age and significance, Geophys. Res. Lett., 41, 2794–2802,doi:10.1002/2014GL059439, 2014.

Skinner, L.C., and I.N. McCave, Analysis and modeling of gravity and piston coring based on soil mechanics. Marine Geology, 199, 181-204, 2003.

Skinner, L.C., N.J. Shackleton and H. Elderfield, Millennial-scale variability of deep-water temperature and $\delta^{18}O_{dw}$ indicating deep-water source variations in the Northeast Atlantic, 0-34 cal. ka BP. Geochem. Geophys. Geosys. 4, 1-17, 2003.

Skinner, L.C. and N.J. Shackleton, Rapid transient changes in Northeast Atlantic deep-water ventilation-age across Termination I. Paleoceanography 19, 1-11, 2004.

Skinner, L.C., H. Elderfield and M. Hall, Phasing of millennial events and Northeast Atlantic deep-water temperature change since ~ 50 ka BP, in: Schmittner, A., Chiang, J., Hemming, S.R. (Eds.), Ocean Circulation: Mechanisms and Impacts. AGU Monograph, pp. 197-208, 2007.

Skinner, L.C., S. Fallon, C. Waelbroeck, E. Michel and S. Barker, Ventilation of the deep Southern Ocean and deglacial CO2 rise. Science 328, 1147-1151, 2010.

Skinner, L.C., C. Waelbroeck, A. Scrivner and S. Fallon, Radiocarbon evidence for alternating northern and southern sources of ventilation of the deep Atlantic carbon pool during the last deglaciation. Proc. Nat. Acad. Sci., 111, 5480–5484, 2014.

Skinner, L., I.N. McCave, L. Carter, S. Fallon, A. Scrivner and F. Primeau, Reduced ventilation and enhanced magnitude of the deep Pacific carbon pool during the last glacial period. Earth Planet. Sci. Lett. 411, 45-52, 2015.

Southon, J., A.L., Noronha, H. Cheng, R.L. Edwards and Y. Wang, A high-resolution record of atmospheric ^{14}C based on Hulu Cave speleothem H82. Quaternary Science Reviews 33, 32-41, doi:https://doi.org/10.1016/j.quascirev.2011.11.022, 2012.

Stoner, J.S., C. Laj, J.E.T. Channell and C. Kissel. South Atlantic (SAPIS) and North Atlantic (NAPIS) geomagnetic paleointensity stacks (0-80 ka): implications for inter-hemispheric correlation. Quaternary Science Reviews, 21, 1141-1151, 2002.

Stoner, J.S., J.E.T. Channell, D. A. Hodell and C. Charles. A 580 kyr paleomagnetic record from the sub-Antarctic South Atlantic (ODP Site 1089). J. Geophys. Res., 108, 2244, doi:10.1029/2001JB001390, 2003.

Stott, L., C. Poulsen, S. Lund and R. Thunell, Super ENSO and global climate oscillations at millennial timescles. Science, 297, 222-226, 2002.

Svensson, A. et al., A 60 000 year Greenland stratigraphic ice core chronology. Climate of the Past 4, 47-57, doi:10.5194/cp-4-47-2008, 2008.

Széréméta, N., F. Bassinot, Y. Balut, L. Labeyrie and M. Pagel, Oversampling of sedimentary series collected by giant piston corer: Evidence and corrections based on 3.5-kHz chirp profiles. Paleoceanography, 19, PA1005, doi:10.1029/2002PA000795, 2004.

Tauxe, L., Sedimentary records of relative paleointensity of the geomagnetic field: theory and practice. Rev. Geophys., 31, 319-354, 1993.

Teanby, N., C. Laj, D. Gubbins and M. Pringle, A detailed palaeointnesity and inclination record from drill core SOH1 on Hawaii. Phys. Earth Planet. Int., 131, 101-140, 2002.

Thomas, R., Y. Guyodo and J.E.T. Channell, U-channel track for susceptibility measurements. Geochemistry, Geophysics and Geosystems (G^3), 1050, doi: 10.1029/2002GC000454, 2003.

Thomson, J., S. Nixon, C. P. Summerhayes, J. Schonfeld, R. Zahn, and P. Grootes, Implications for sedimentation changes on the Iberian margin over the last two glacial/interglacial transitions from ($^{230}Th_{excess}$) systematics, Earth Planet. Sci. Letts. 165, 255-270, 1999.

Thomson, J., S. Nixon, C. P. Summerhayes, E. J. Rohling, J. Schonfeld, R. Zahn, P. Grootes, F. Abrantes, L. Gaspar, and S. Vaqueiro, Enhanced productivity on the Iberian margin during glacial/interglacial transitions revealed by barium and diatoms, J. Geol. Soc., 157, 667-677, 2000.

Thouveny, N., K.M. Creer and D. Williamson, Geomagnetic moment variations in the last 70,000 years, impact on production of cosmogenic isotopes. Global and Planet. Change, 7, 157-172, 1993.

Thouveny, N., Carcaillet, J., Moreno, E., Leduc, G., and Nerini, D., Geomagnetic moment variation and paleomagnetic excursions since 400 kyr BP; a stacked record from sedimentary sequences of the Portuguese margin. Earth Planet. Sci. Lett., 219: 377-396, 2004.

Umling, N.E. and R.C. Thunell, Synchronous deglacial thermocline and deep-water ventilation in the eastern equatorial Pacific. Nature Communications 8, 14203, 2017.

Yiou, F., Raisbeck, G.M., Baumgartner, S., Beer, J., Hammer, C., Johnsen, S., Jouzel, J., Kubik, P.W., Lestringuez, J., Stiévenard, M., Suter, M., Yiou, P., Beryllium-10 in the Greenland Ice Core Project ice core at Summit, Greenland. J. Geophys. Res. 102, 26783–26794, 1997.

Valet, J.-P., L. Meynadier and Y. Guyodo, Geomagnetic dipole strength and reversal rate over the past two million years. Nature 435, 802-805, 2005.

Vigliotti, L., J.E.T. Channell and M. Stockhecke, Paleomagnetism of Lake Van sediments: chronology and paleoenvironment since 350 ka. Quat. Sci. Revs., 104, 18-29, 2014.

Wagner, G., J. Beer, C. Laj, C. Kissel, J. Masarik, R. Muscheler, H.-A. Synal, Chlorine-36 evidence for the Mono Lake event in the Summit GRIP ice core. Earth and

796 Planetary Science Letters 181, 1–6, 2000.
797 Wang, Y.J., H. Cheng, R.L. Edwards, Z.S. An, J.Y. Wu, C.-C. Shen, J.A. Dorale, A high-
798 resolution absolute-dated Late Pleistocene monsoon record from Hulu Cave, China,
799 Science 294, 2345–2348, 2001.
800 Weeks, R., C. Laj, L. Endignoux, M. Fuller, A. Roberts, R. Manganne, E. Blanchard, and
801 W. Goree, Improvements in long-core measurement techniques: applications in
802 palaeomagnetism and palaeoceanography. Geophys. J. Int., 114, 651-662, 1993.
803 Xiao, W., T. Frederichs, R. Gersonde and G. Kuhn, Constraining the dating of late
804 Quaternary marine sediment records from the Scotia Sea (Southern Ocean). Quat.
805 Geochron., 31, 97-118, 2016.
806 Xuan, C. and J.E.T. Channell, UPmag: MATLAB software for viewing and processing u-
807 channel or other pass-through paleomagnetic data. Geochem. Geophys. Geosyst., 10,
808 Q10Y07, doi:1029/2009GC002584, 2009.
809 Xuan, C., J.E.T. Channell and D.A. Hodell, Quaternary paleomagnetic and oxygen
810 isotope records from diatom-rich sediments of the southern Gardar Drift (IODP Site
811 U1304, North Atlantic). Quaternary Science Reviews, 142, 74-89, 2016.
812 Zangger, E. and I.N. McCave, A redesigned kasten core barrel and sampling technique.
813 Marine Geology, 94, 165-171, 1990.
814 Ziegler, L.B., C.G. Constable, C.L. Johnson and L. Tauxe, PADM2M: a penalized
815 maximum likelihood model of the 0-2 Ma paleomagnetic axial dipole moment.
816 Geophys. J. Int., 184, 1069-1089, 2011.
817
818

819 Figure Captions
820
821 Fig. 1 (a) Relative paleointensity stacks: NAPIS (blue, Laj et al., 2000), GLOPIS (orange,
822 Laj et al., 2004), SAPIS (dark green, Stoner et al., 2003), Sint-2000 (dashed red, Valet et
823 al., 2005), PISO-1500 (dashed black, Channell et al., 2009) and PADM2M (dashed light
824 green, Ziegler et al., 2011). (b) Modeled Holocene axial dipole field intensity (brown,
825 Korte et al., 2011; black, Pavon-Carrasco et al., 2014), virtual axial dipole moment
826 (VADM) determined from ^{10}Be flux (blue) and ^{36}Cl flux (green) in Greenland ice cores
827 (Muscheler et al., 2005), and from Δ^{14}C (red dashed, Muscheler et al., 2005).
828
829 Fig. 2. Location of stations (3-8) occupied during cruise JC089 (Table 1), and
830 neighboring cores (MD95-2042 and MD01-2444, Table 2). Core MD01-2444 and Station
831 6 are nominally at the same location.
832
833 Fig. 3. (a) Ca/Ti ratio from XRF core scans of piston cores (blue) and Kasten cores (red)
834 correlated to the L* reflectance from Cariaco Basin (black) from Deplazes et al. (2013)
835 for the 0-50 ka interval. (b) Ca/Ti ratio from XRF core scans for the 12-18 ka interval. (c)
836 Zr/Sr ratio from XRF core scans for the 12-18 ka interval. Piston cores shown in blue,
837 Kasten cores shown in red with labeled records from core 06-4K (light green), 06-5K
838 (dark green) and 05-3K. Younger Dryas (YD), Bølling-Allerød (BA), Heinrich stadials
839 (HS1-HS5) are marked.
840
841 Fig. 4. Component declination, inclination and associated maximum angular deviation
842 (MAD) values determined for a uniform 20-80 mT peak field demagnetization interval.
843 Piston cores 05-3P (green) and 03-1P (black) show variable declinations in the upper
844 part. Other piston cores shown in blue, and Kasten cores in red. Cores were not oriented
845 in azimuth, and the declinations were set by uniform rotation of the mean declination for
846 each core to 0°.
847
848 Fig. 5 (a) Examples of orthogonal projection of AF demagnetization of natural remanent
849 magnetization (NRM) for u-channel samples from JC089 Kasten cores. Examples from

850 piston cores are shown in Figure S7. Projections are shown for core depths of 100 cm,
851 200 cm, 250 cm and 350 cm (300 cm usually corresponds to a section break). Peak fields
852 are 0, 10-30 mT in 5mT steps, 30-60 mT in 2.5 mT steps and 60-80 mT in 5 mT steps.
853 Intensities are given in mA/m. (b) Normalized intensities for NRM (black), ARM (blue),
854 $IRM_{0.3T}$ (orange), and IRM_{1T} (red) at core depths of 100 cm and 200 cm in Cores 03-6K,
855 04-2K and 05-3K.
856
857 Fig. 6. (a) Plot of anhysteretic susceptibility (κ_{arm}) versus susceptibility (κ) with lines
858 indicating lines of equal magnetite grain-size after King et al. (1983). (b) Hysteresis ratio
859 plot for JC089 piston core data (blue) and JC089 Kasten core data (red) after Day et al.
860 (1977) with magnetite grain size mixing line (green) from Carter-Stiglitz et al. (2001),
861 and data for unannealed sized magnetite (Dunlop, 2002; Carter-Stiglitz and Dunlop,
862 2006). (c) Susceptibility (κ) versus age for JC089 piston cores (blue) and JC089 Kasten
863 cores (red) with core 07-4P labeled. (d) κ_{arm}/κ versus age for JC089 piston cores (blue)
864 and JC089 Kasten cores (red) with cores 06-4K and 07-4P labeled. (e) S-ratios
865 determined as the ratio of $IRM_{0.3T}$ over IRM_{1T} (both after AF demagnetization at peak
866 fields of 30 mT) for a selection of JC089 Kasten cores (red) and piston cores (blue).
867 Labeling of Younger Dryas (YD) and Heinrich stadials: see caption of Figure 3.
868
869 Fig. 7. Sedimentation rates, and relative paleointensity (RPI) proxies for Cores 06-4K,
870 06-5K and MD01-2444. Slopes and accompanying linear correlation coefficients (r):
871 NRM/ARM (dark blue), NRM/ARMAQ (light blue), $NRM/IRM_{0.3T}$ (orange),
872 NRM/IRM_{1T} (red). Core MD01-2444 RPI proxy (black) and sedimentation rates (red)
873 from Channell et al. (2013). Yellow shading indicates RPI minimum at ~13.5 ka. Grey
874 shading indicates last 2 kyr (unreliable surface sediment).
875
876 Fig. 8. Sedimentation rates, and relative paleointensity (RPI) proxies for (a) Cores 03-1P
877 and 03-6K, (b) Cores 04-2P and 04-2K, (c) Cores 05-3P and 05-3K, (d) Cores 07-4P and
878 08-5P. Slopes and accompanying linear correlation coefficients (r): NRM/ARM (dark
879 blue), NRM/ARMAQ (light blue), $NRM/IRM_{0.3T}$ (orange), NRM/IRM_{1T} (red). Yellow

shading indicates RPI minimum at ~13.5 ka. Grey shading indicates last 2 kyr (unreliable surface sediment).

Fig. 9. Relative paleointensity data: (a) Iberian Margin stack (red), the stack from outside the Iberian Margin (blue) and an overall stack (black, see text for details) with the Holocene models of Korte et al. (2011) (brown) and Pavon-Carrasco et al. (2014) (black). Error bars on stacks are standard errors (2σ). (b) Individual Iberian Margin records from piston cores (blue) and Kasten cores (red) with Core MD01-2444 data (black continuous line, Channell et al., 2013) and the Portuguese Margin Stack (green, Thouveny et al., 2004). The black dashed line represents the Iberian Margin stack. (c) Individual records from outside the Iberian Margin (Table 2) including records from the South Atlantic realm (red), western Pacific realm (green), North Atlantic (blue) and Europe/Mediterranean (black). Black dashed line is the resulting stack for records from outside the Iberian Margin. Yellow shading marks RPI minima at ~13.5 ka, 26.5 ka (Rockall excursion), 34 ka (Mono Lake excursion) and 41 ka (Laschamp excursion). Grey shading indicates last 2 kyr (unreliable surface sediment).

Fig. 10. The overall virtual axial dipole (VADM) geomagnetic stack from Figure 9a (black with 2σ error) with the Holocene model of Korte et al. (2011) (green) plotted with an updated calculation of the ^{10}Be-based VADM (blue) and ^{14}C-based VADM (red). The updated VADM calculations from ^{14}C and ^{10}Be, in contrast to Figure 1b (from Muscheler at al., 2005), are based on the most recent Greenland ice-core time scale (Svensson et al., 2008). The ^{10}Be-based curve was calculated after low-pass filtering (cut-off 1/3000 yrs) the revised ^{10}Be flux, and by using the most recent ^{10}Be production models (Poluianov et al., 2016; Herbst et al., 2017).

Fig. 11 (a) Comparison of the Intcal13 ^{14}C data (black, Reimer et al., 2013) and modeled Δ^{14}C based on the overall VADM stack (labeled PI), and the ^{10}Be-based VADM, using a box-diffusion carbon cycle model (Siegenthaler, 1983) where the solid blue curve includes no magnetization lock-in delay and the dashed light blue curve includes a 2 kyr lock-in delay. The conversion of geomagnetic field into ^{14}C production rates was

911 achieved using the local interstellar cosmic ray spectrum of Herbst et al. (2017) and the
912 cosmogenic radionuclide yield functions of Poluianov et al. (2016). (b) Selected
913 published marine radiocarbon ventilation records from the North Atlantic (red line and
914 stars; Skinner et al., 2014), South Atlantic (black line and crossed diamonds; Skinner et
915 al., 2010), South Pacific (purple filled diamonds; Skinner et al., 2015), and Eastern
916 Equatorial Pacific (purple line and crossed squares; de la Fuente et al., 2015) compared
917 with the 'expected' mean ocean ventilation age derived from the observed and modeled
918 atmospheric radiocarbon activities in (a), assuming that their offset up to 5 ka is
919 accounted for by mass balance of radiocarbon in the ocean-atmosphere system. (c)
920 Comparison of atmospheric pCO_2 (Monnin et al., 2001; Lemieux-Dudon et al., 2010) and
921 offsets between the observed and modeled $\Delta^{14}C$ records shown in (a). The mass balance
922 calculation assumes that changes in the marine and atmospheric radiocarbon inventories
923 form a closed and conservative system such that:
924 $$-\Delta R_a.XCO_2.M_a = \Delta R_o.C_o.V_o$$
925 where ΔR_a and ΔR_o are incremental changes in the atmospheric- and average ocean
926 radiocarbon activities, XCO_2 is the molar mixing ratio of the atmosphere (assumed
927 equivalent to partial pressure at a nominal pressure of 1 atm), M_a is the molar mass of the
928 atmosphere, C_o is the average carbon concentration of the ocean (assumed invariant at
929 ~2.28352 mol/m^3), and V_o is the volume of the ocean (assumed to equal to 1.3 x 10^8 m^3).
930 Incremental changes in R_a were derived at 200 yr time-steps and summed up forward in
931 time.
932
933 Supplementary Fig. S1. Log(Ca/Ti) of JC089 cores from the Iberian Margin cores
934 correlated to L* of Cariaco Basin for 0 to 80 ka (Deplazes et al., 2013). Individual
935 records have been offset by a constant for illustration purposes.
936
937 Supplementary Fig. S2. Log(Ca/Ti) of JC089 cores from the Iberian Margin cores
938 correlated to L* of Cariaco Basin for 0 to 25 ka (Deplazes et al., 2013). Individual
939 records have been offset by a constant for illustration purposes.
940

941 Supplementary Fig. S3. Log(Zr/Sr) of JC089 cores from the Iberian Margin cores
942 correlated to L* of Cariaco Basin for 0 to 80 ka (Deplazes et al., 2013). Individual
943 records have been offset by a constant for illustration purposes.
944
945 Supplementary Fig. S4. Log(Zr/Sr) of JC089 cores from the Iberian Margin cores
946 correlated to L* of Cariaco Basin for 0 to 25 ka (Deplazes et al., 2013). Individual
947 records have been offset by a constant for illustration purposes.
948
949 Supplementary Fig. S5. Tie points and sedimentation rates for piston (filled circles) and
950 kasten (filled squares) cores from the Iberian Margin based on correlating XRF Ca/Ti and
951 Zr/Sr to Cariaco L* for 0 to 80 ka. Open squares are the tie points used by Freeman et al.
952 (2016).
953
954 Supplementary Fig. S6. Tie points and sedimentation rates for piston (filled circles) and
955 kasten (filled squares) cores from the Iberian Margin based on correlating XRF Ca/Ti and
956 Zr/Sr to Cariaco L* for 0 to 25 ka. Open squares are the tie points used by Freeman et al.
957 (2016).
958
959 Supplementary Fig. S7. Examples of orthogonal projections of AF demagnetization of
960 natural remanent magnetization (NRM) for JC089 piston cores. Projections for core
961 depths of 100 cm, 200 cm, 250 cm and 350 cm (300 cm usually corresponds to a section
962 break). Peak fields are 0, 10-30 mT in 5mT steps, 30-60 mT in 2.5 mT steps and 60-80
963 mT in 5 mT steps. Intensities are given in mA/m.
964
965 Supplementary Table 1. The overall relative paleointensity (RPI) stack, scaled to virtual
966 axial dipole moment (VADM).
967
968 Supplementary Table 2. Geomagnetic intensity proxy based on ^{10}Be flux in Greenland ice
969 cores, resampled at 0-5 kyr intervals, using the GICC05 timescale of Svensson et al.
970 (2008).
971

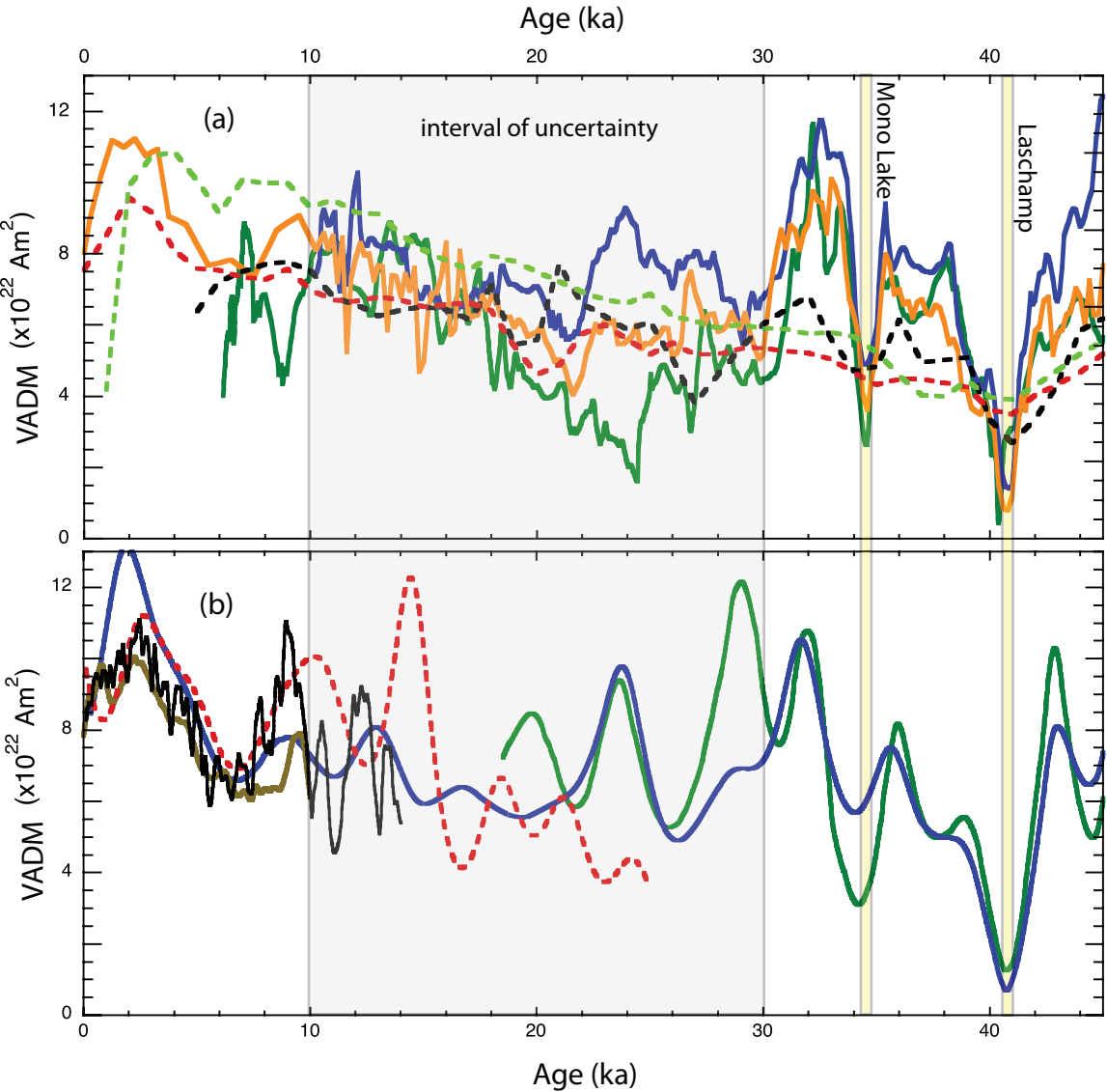
Age (ka)
0
10
20
30
40
(a)
interval of uncertainty
Mono Lake
Laschamp
VADM (x10^22 Am^2)
12
8
4
0
(b)
VADM (x10^22 Am^2)
12
8
4
0
Age (ka)

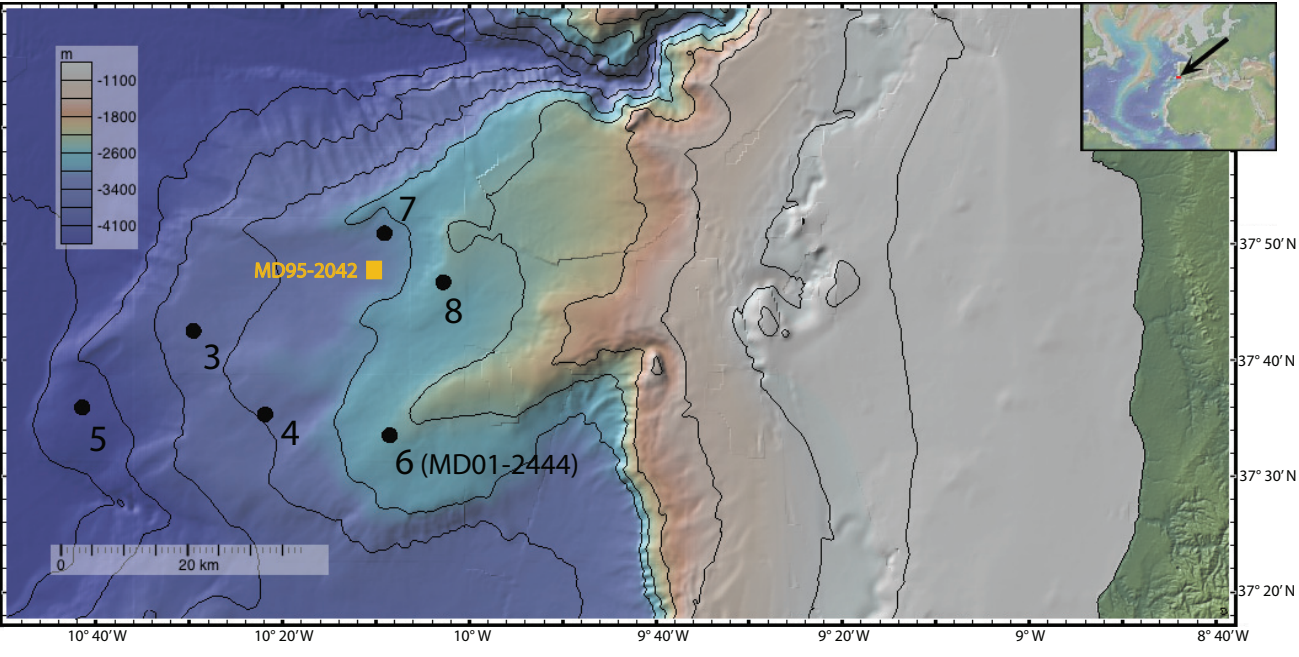
m
-1100
-1800
-2600
-3400
-4100
MD95-2042
7
8
3
4
5
6 (MD01-2444)
0
20 km
37° 50′ N
37° 40′ N
37° 30′ N
37° 20′ N
10° 40′ W
10° 20′ W
10° W
9° 40′ W
9° 20′ W
9° W
8° 40′ W

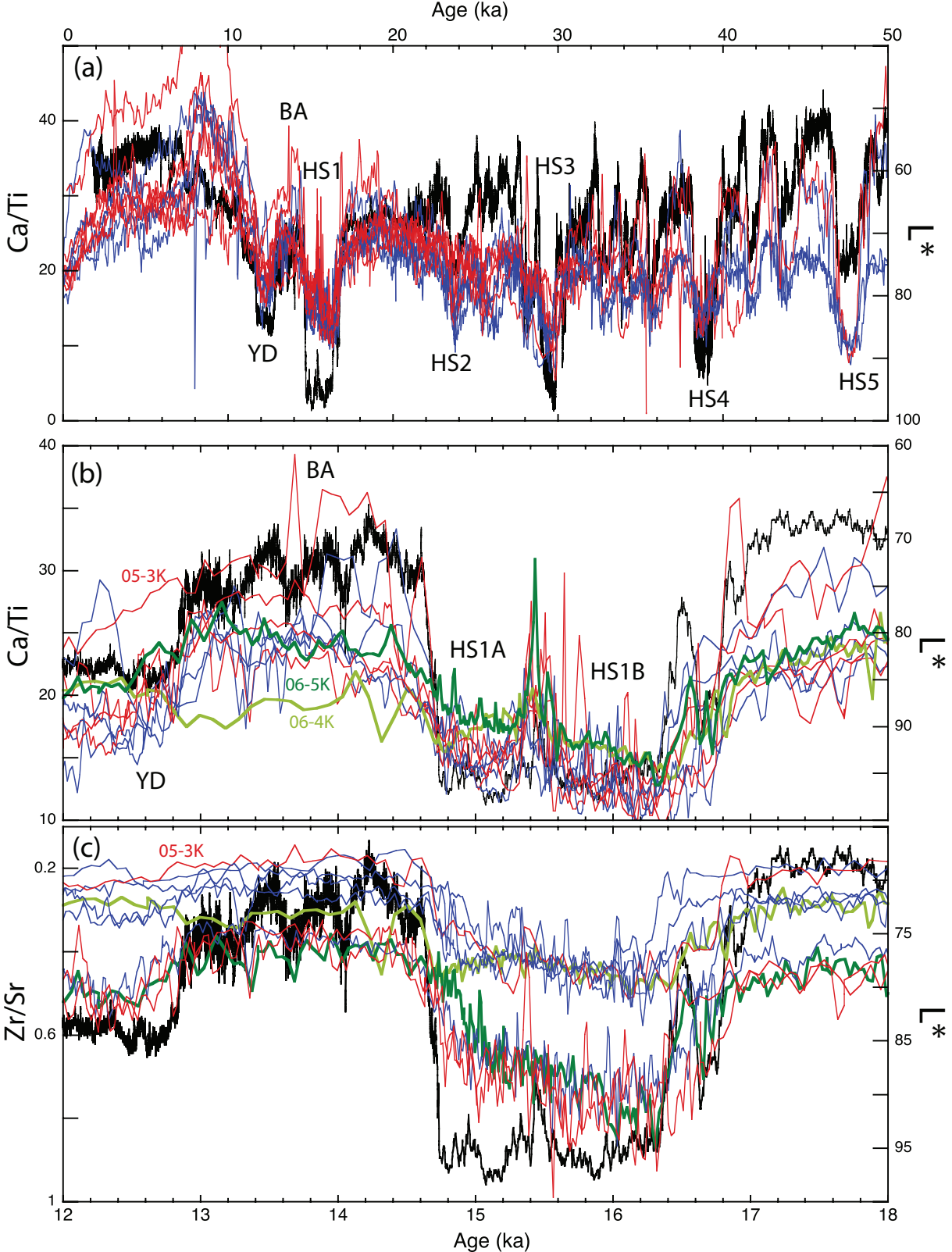
Age (ka)
(a)
BA
HS1
HS3
YD
HS2
HS4
HS5
Ca/Ti
L*
(b)
BA
05-3K
HS1A
HS1B
06-5K
06-4K
YD
Ca/Ti
L*
(c)
05-3K
Zr/Sr
L*
Age (ka)

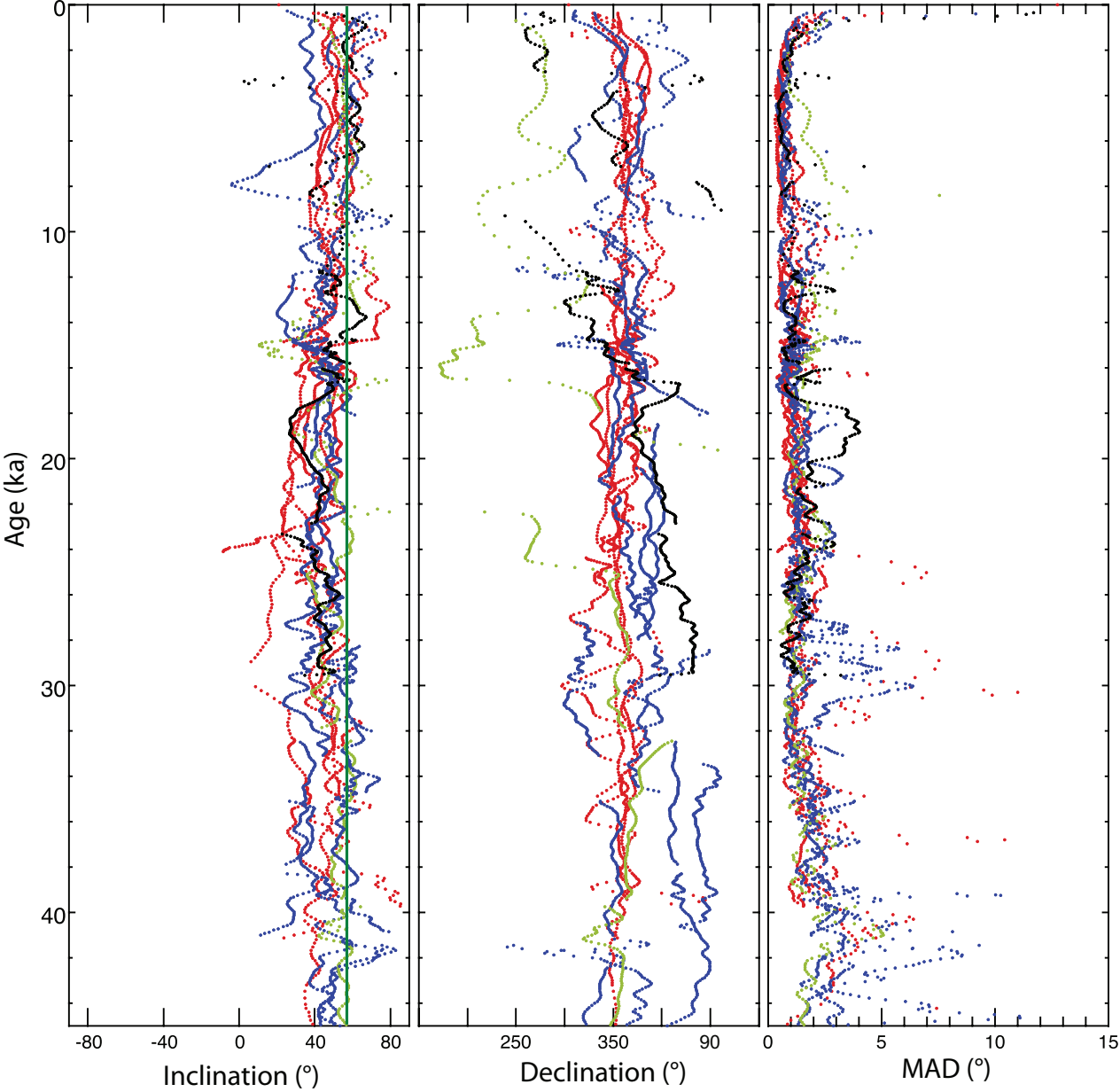
Age (ka)
0
10
20
30
40
-80
-40
0
40
80
Inclination (°)
250
350
90
Declination (°)
0
5
10
15
MAD (°)

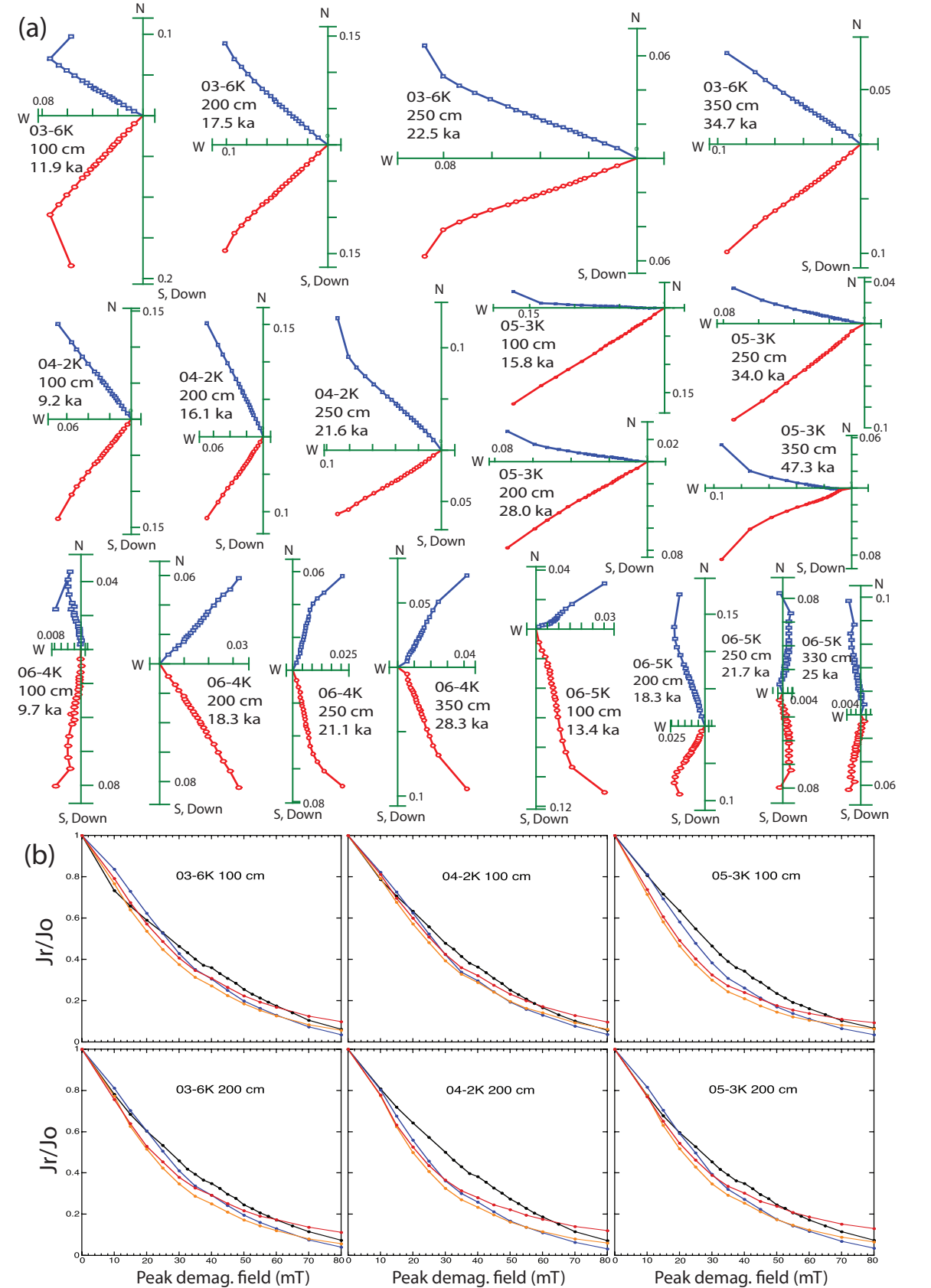
(a)
03-6K
100 cm
11.9 ka
03-6K
200 cm
17.5 ka
03-6K
250 cm
22.5 ka
03-6K
350 cm
34.7 ka
04-2K
100 cm
9.2 ka
04-2K
200 cm
16.1 ka
04-2K
250 cm
21.6 ka
05-3K
100 cm
15.8 ka
05-3K
250 cm
34.0 ka
05-3K
200 cm
28.0 ka
05-3K
350 cm
47.3 ka
06-4K
100 cm
9.7 ka
06-4K
200 cm
18.3 ka
06-4K
250 cm
21.1 ka
06-4K
350 cm
28.3 ka
06-5K
100 cm
13.4 ka
06-5K
200 cm
18.3 ka
06-5K
250 cm
21.7 ka
06-5K
330 cm
25 ka
N
W
S, Down
(b)
03-6K 100 cm
04-2K 100 cm
05-3K 100 cm
03-6K 200 cm
04-2K 200 cm
05-3K 200 cm
Jr/Jo
Peak demag. field (mT)

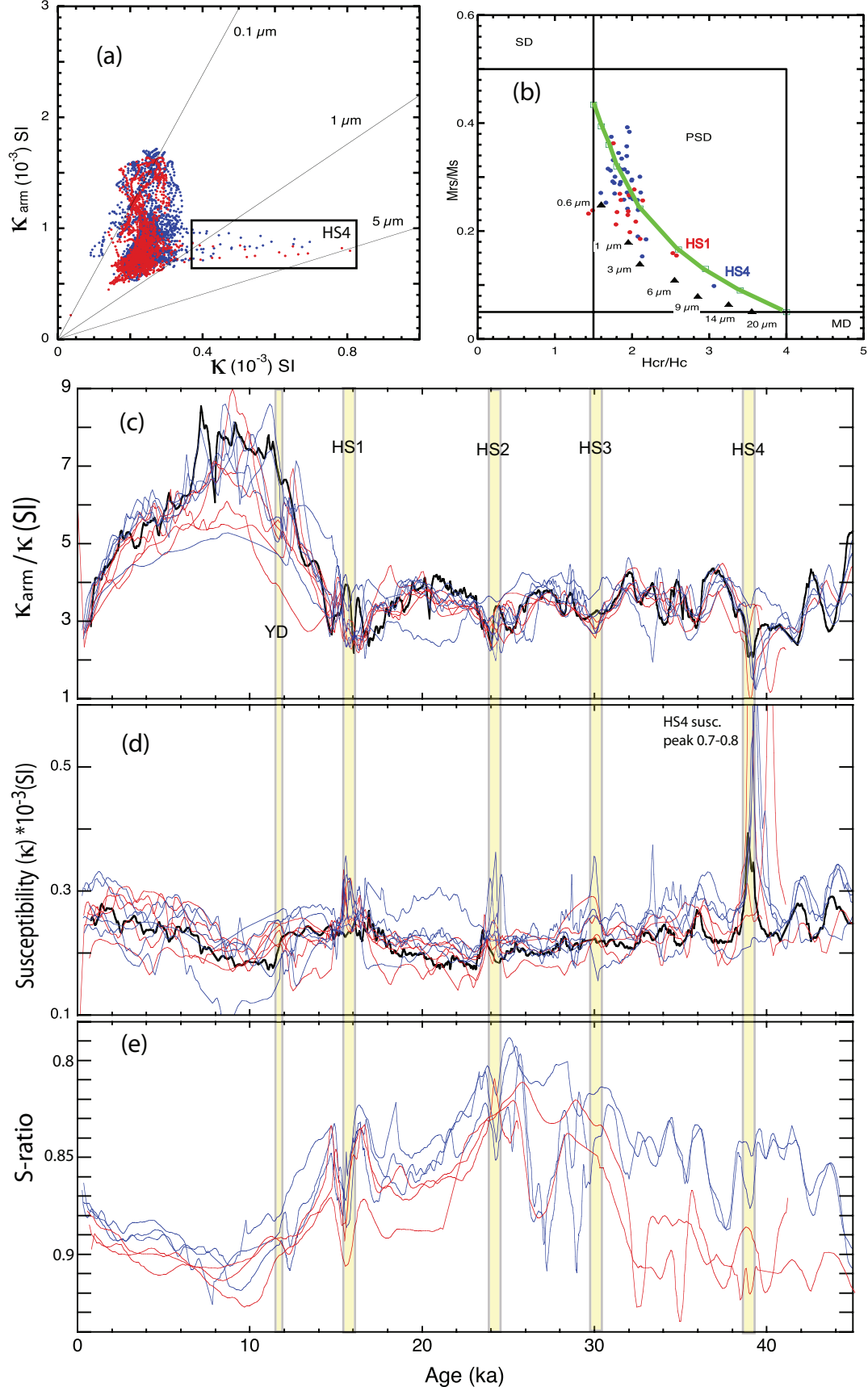
(a)
0.1 μm
1 μm
5 μm
HS4
κarm (10-3) SI
κ (10-3) SI
(b)
SD
PSD
MD
0.6 μm
1 μm
3 μm
6 μm
9 μm
14 μm
20 μm
HS1
HS4
Mrs/Ms
Hcr/Hc
(c)
HS1
HS2
HS3
HS4
YD
κarm /κ (SI)
(d)
HS4 susc.
peak 0.7-0.8
Susceptibility (κ) *10-3(SI)
(e)
S-ratio
Age (ka)

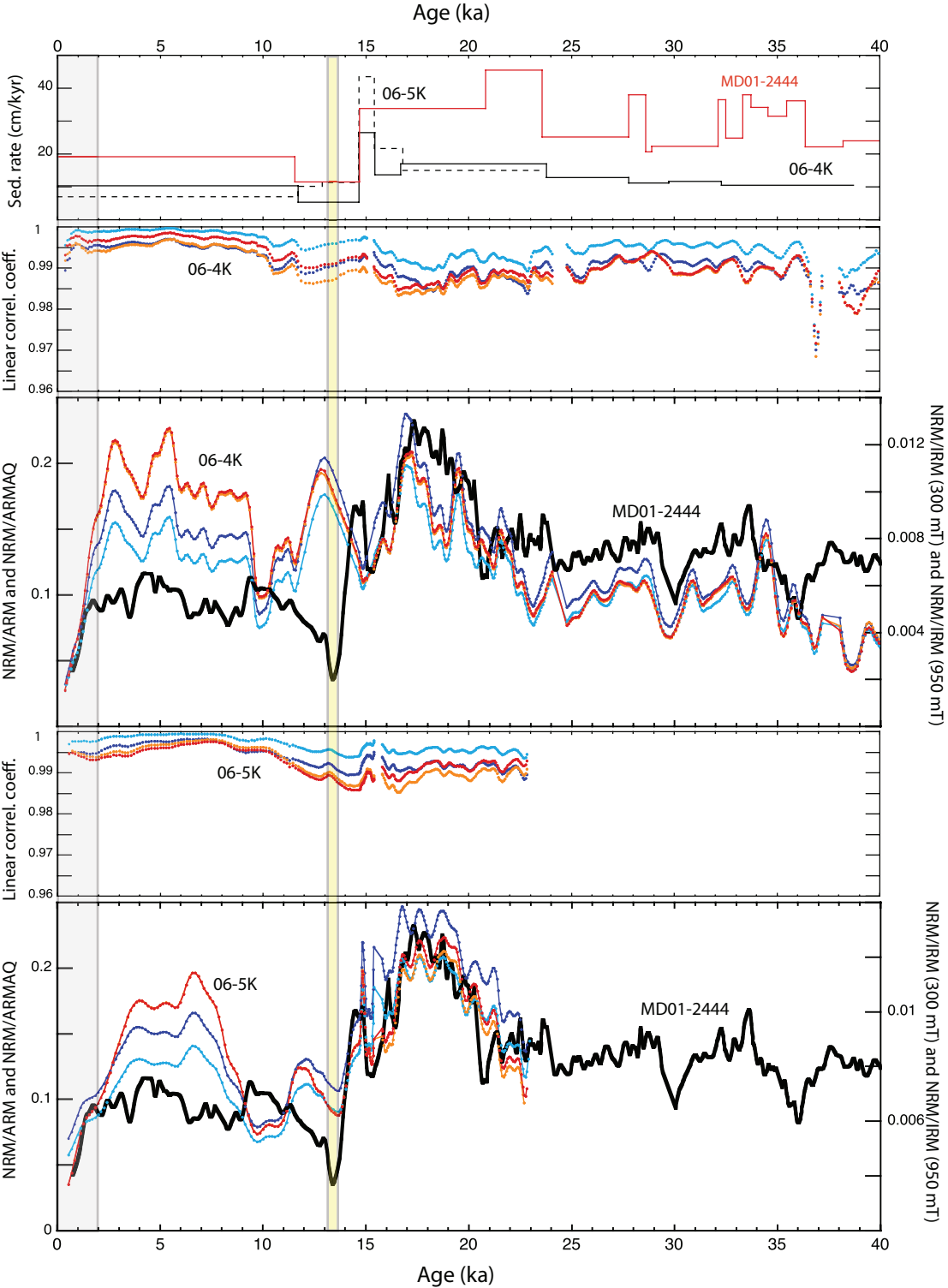
Age (ka)
Sed. rate (cm/kyr)
06-5K
MD01-2444
06-4K
Linear correl. coeff.
NRM/ARM and NRM/ARMAQ
NRM/IRM (300 mT) and NRM/IRM (950 mT)
Age (ka)

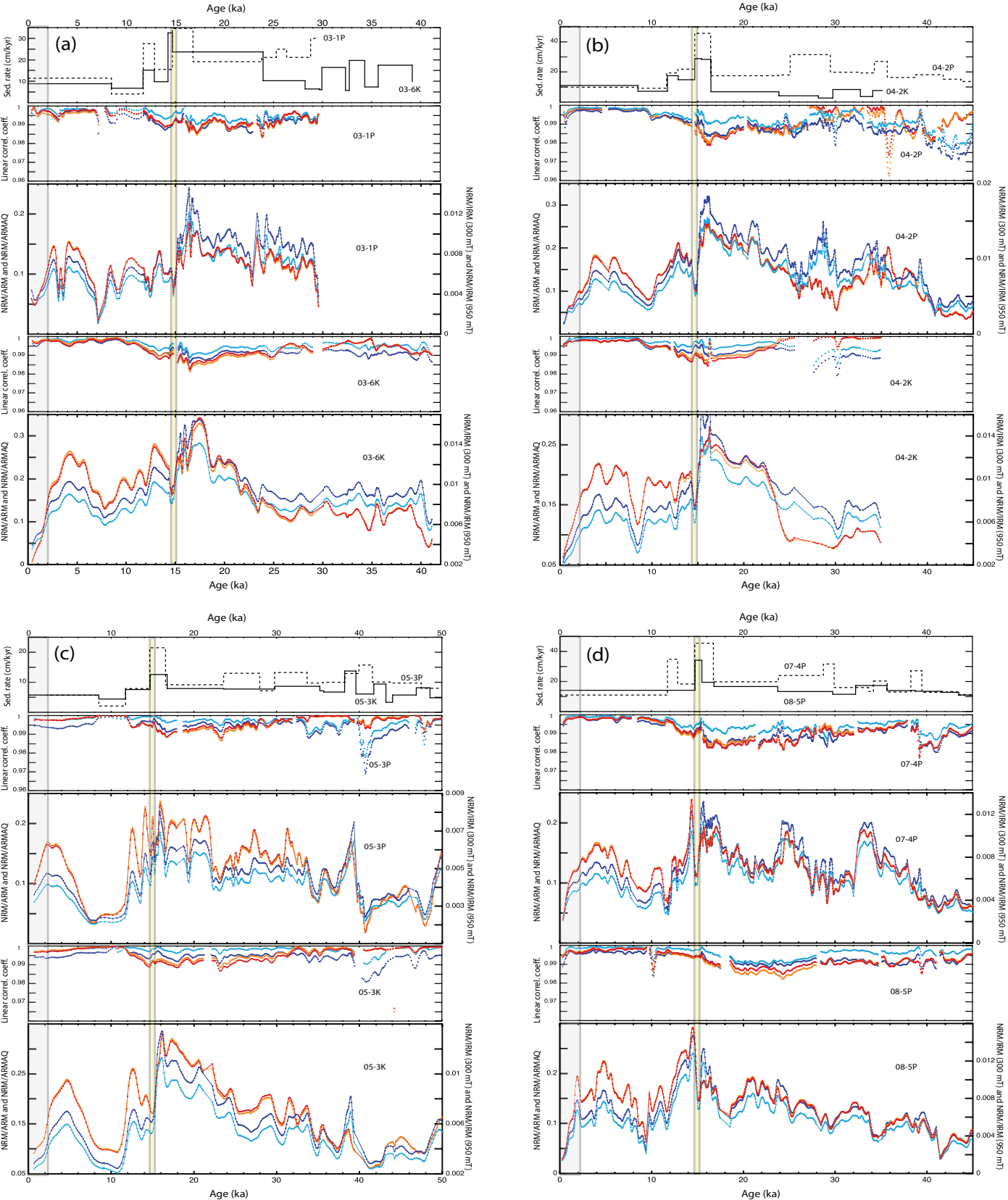
(a)
(b)
(c)
(d)
Age (ka)
Sed. rate (cm/kyr)
03-1P
03-6K
04-2P
04-2K
05-3P
05-3K
07-4P
08-5P
Linear correl. coeff.
NRM/ARM and NRM/ARMAQ
NRM/IRM (300 mT) and NRM/IRM (950 mT)

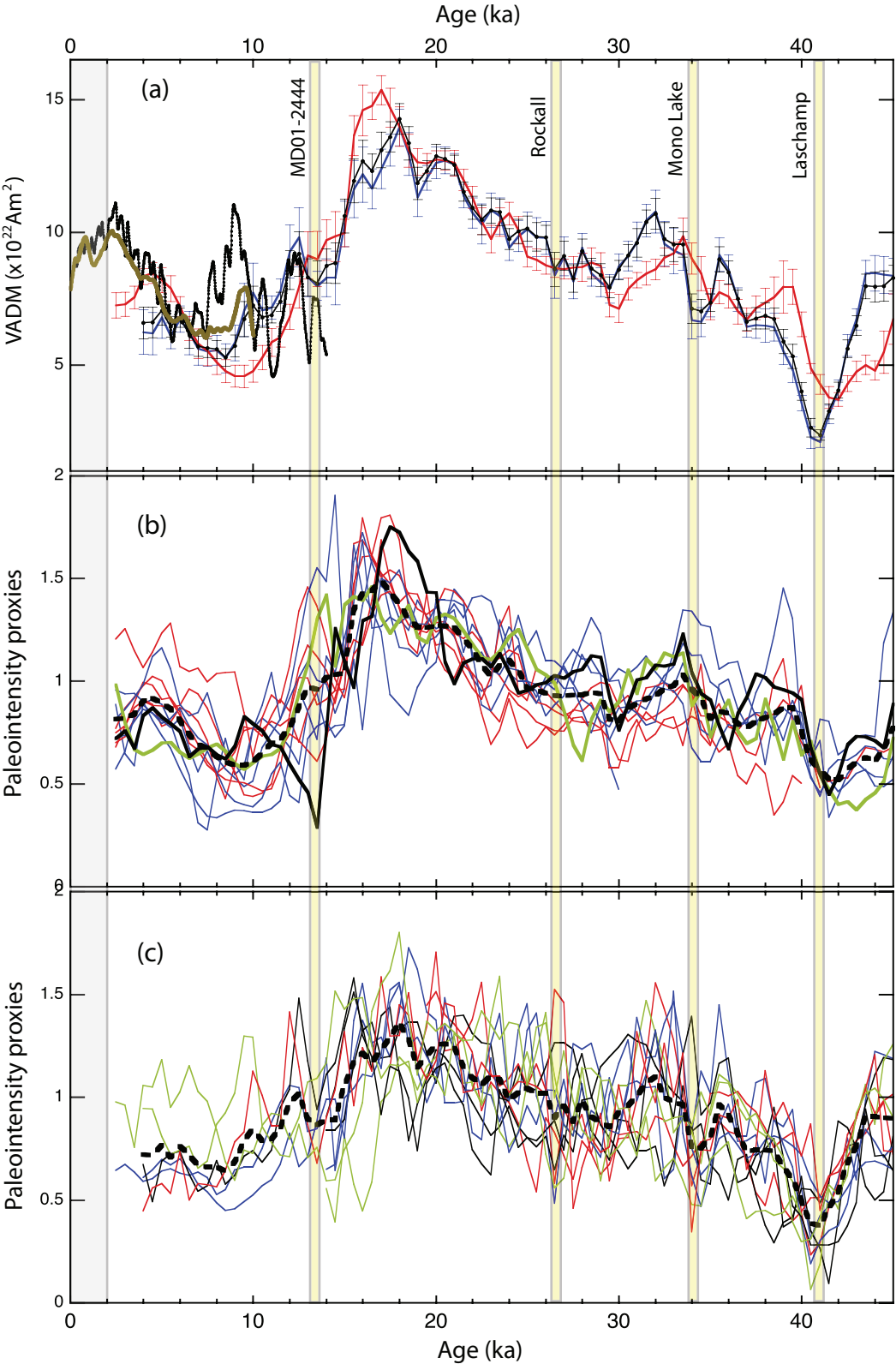
Age (ka)
0
10
20
30
40
(a)
MD01-2444
Rockall
Mono Lake
Laschamp
VADM (x10^{22}Am^2)
15
10
5
2
(b)
Paleointensity proxies
1.5
1
0.5
0
(c)
Paleointensity proxies
1.5
1
0.5
0
0
10
20
30
40
Age (ka)

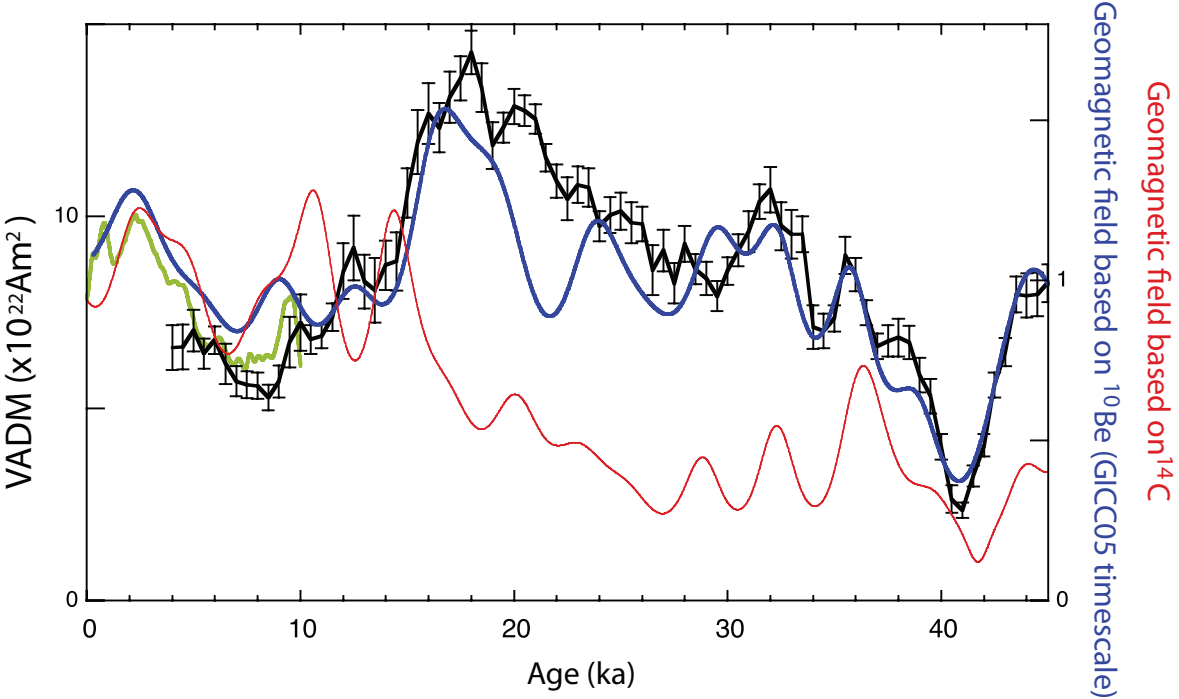
VADM (x10 22 Am 2)
10
0
0
10
20
30
40
Age (ka)
1
0
Geomagnetic field based on 10 Be (GICC05 timescale)
Geomagnetic field based on 14 C

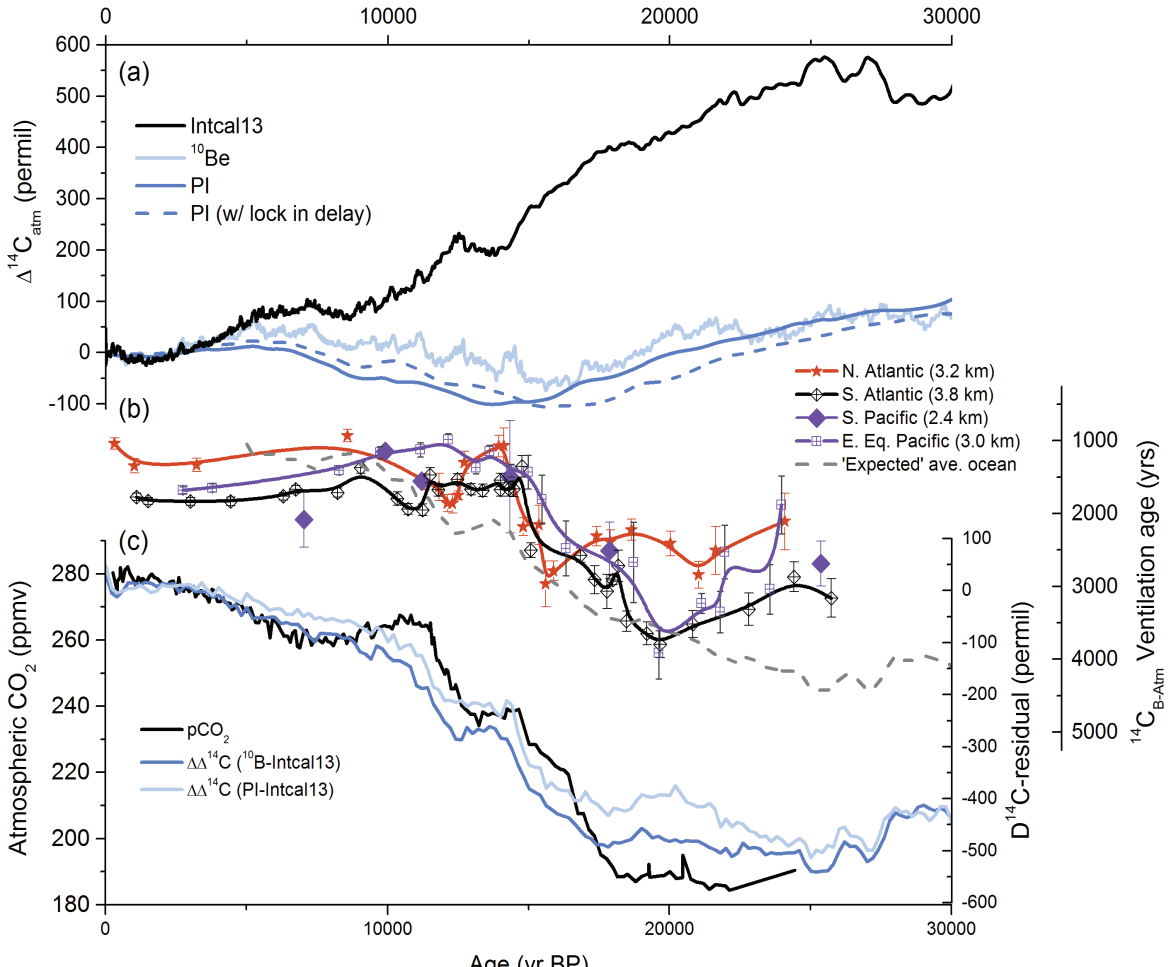
(a)
Intcal13
^{10}Be
PI
PI (w/ lock in delay)
$\Delta^{14}C_{atm}$ (permil)
(b)
N. Atlantic (3.2 km)
S. Atlantic (3.8 km)
S. Pacific (2.4 km)
E. Eq. Pacific (3.0 km)
'Expected' ave. ocean
$^{14}C_{B-Atm}$ Ventilation age (yrs)
(c)
pCO_2
$\Delta\Delta^{14}C$ (^{10}B-Intcal13)
$\Delta\Delta^{14}C$ (PI-Intcal13)
Atmospheric CO_2 (ppmv)
$D^{14}C$-residual (permil)
Age (yr BP)

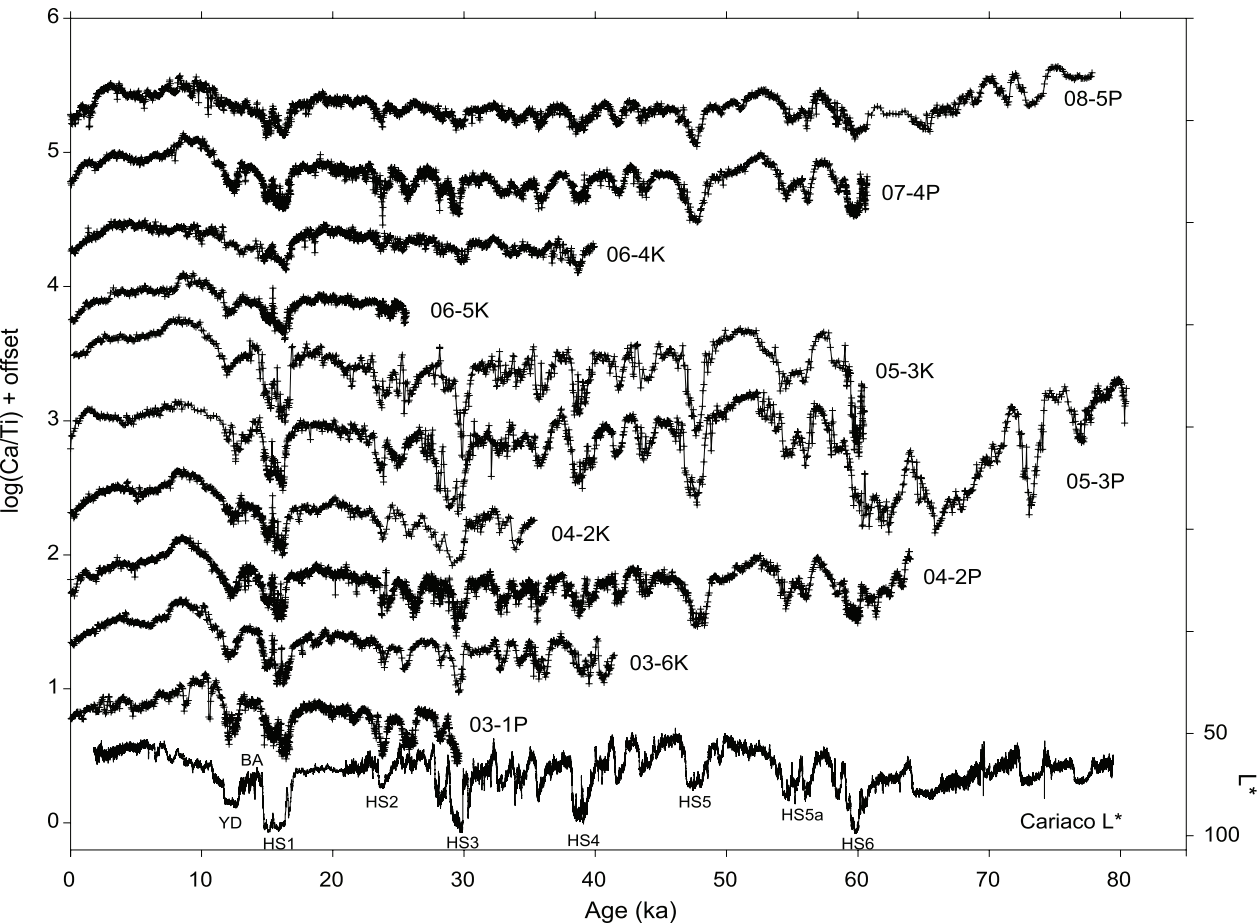
log(Ca/Ti) + offset
Age (ka)
L*
08-5P
07-4P
06-4K
06-5K
05-3K
05-3P
04-2K
04-2P
03-6K
03-1P
Cariaco L*
YD
BA
HS1
HS2
HS3
HS4
HS5
HS5a
HS6

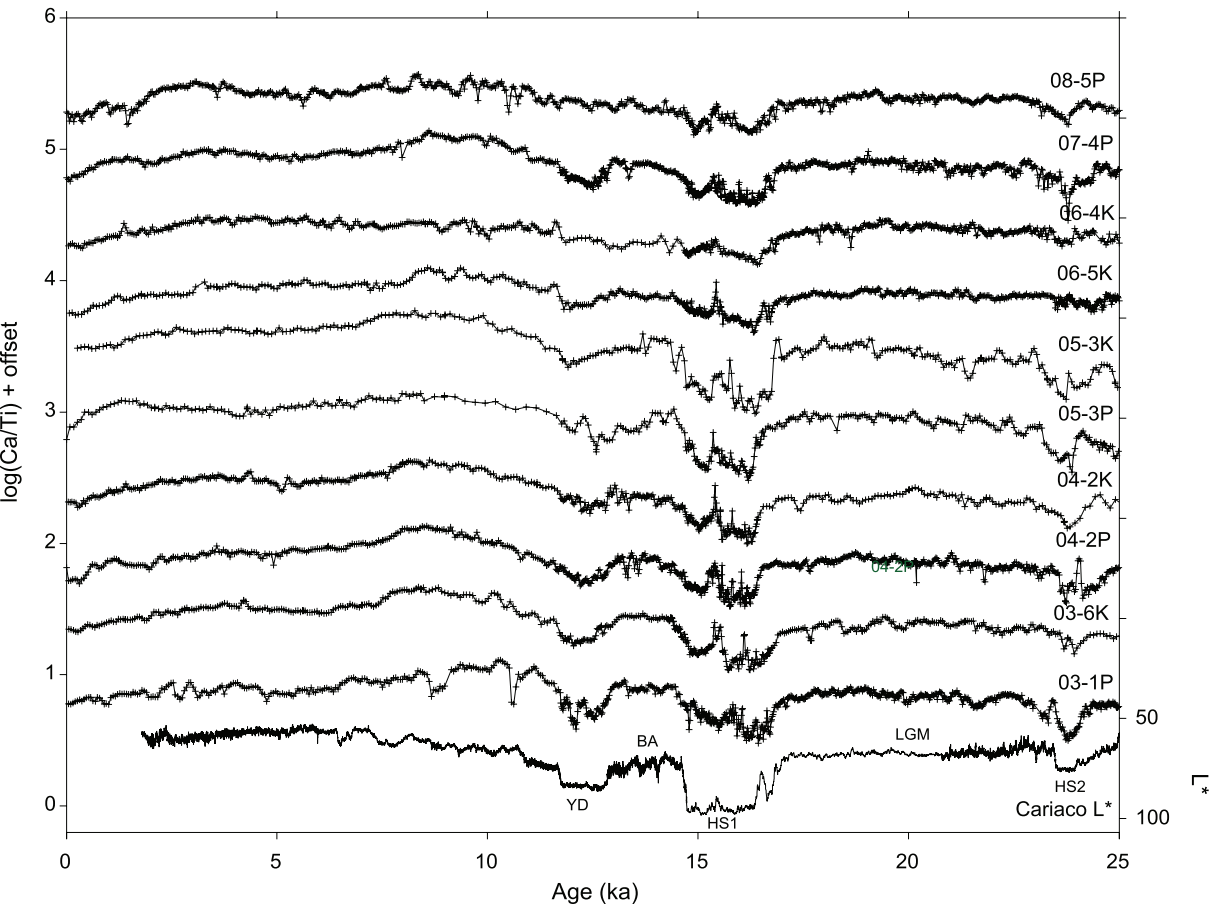
log(Ca/Ti) + offset
Age (ka)
L*
08-5P
07-4P
06-4K
06-5K
05-3K
05-3P
04-2K
04-2P
03-6K
03-1P
Cariaco L*
YD
BA
HS1
LGM
HS2
0
5
10
15
20
25
50
100

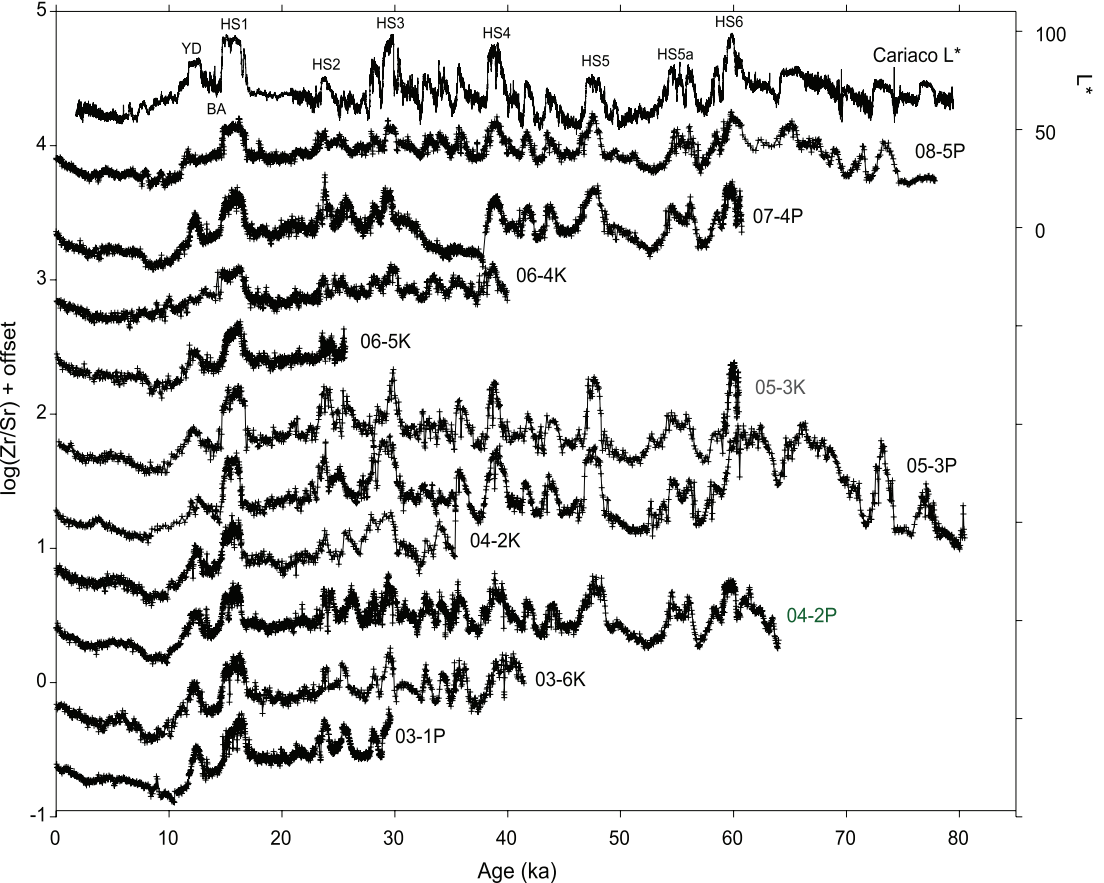
YD
BA
HS1
HS2
HS3
HS4
HS5
HS5a
HS6
Cariaco L*
08-5P
07-4P
06-4K
06-5K
05-3K
05-3P
04-2K
04-2P
03-6K
03-1P
log(Zr/Sr) + offset
Age (ka)
L*

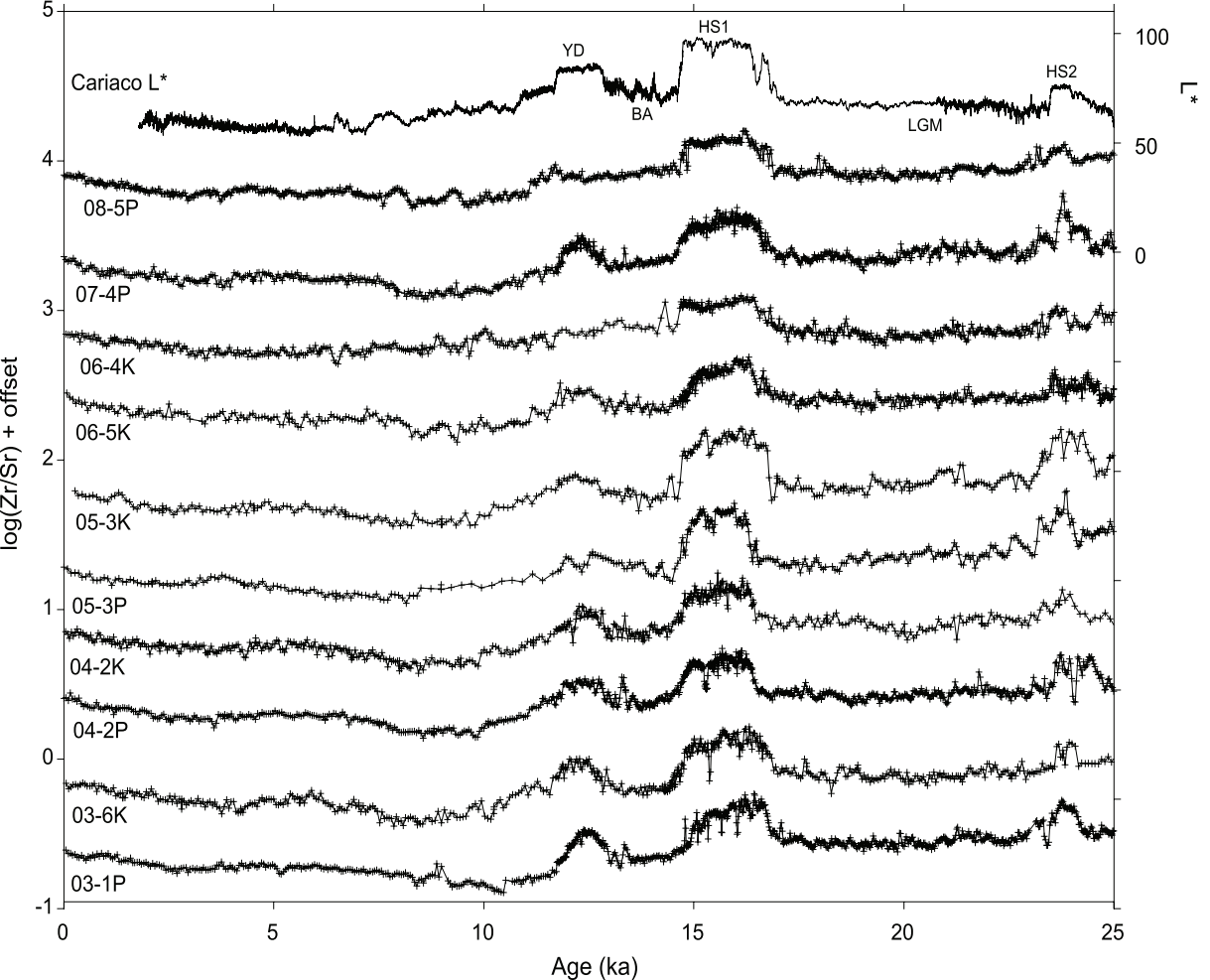
Cariaco L*
YD
HS1
HS2
BA
LGM
08-5P
07-4P
06-4K
06-5K
05-3K
05-3P
04-2K
04-2P
03-6K
03-1P
log(Zr/Sr) + offset
L*
Age (ka)
5
4
3
2
1
0
-1
100
50
0
0
5
10
15
20
25

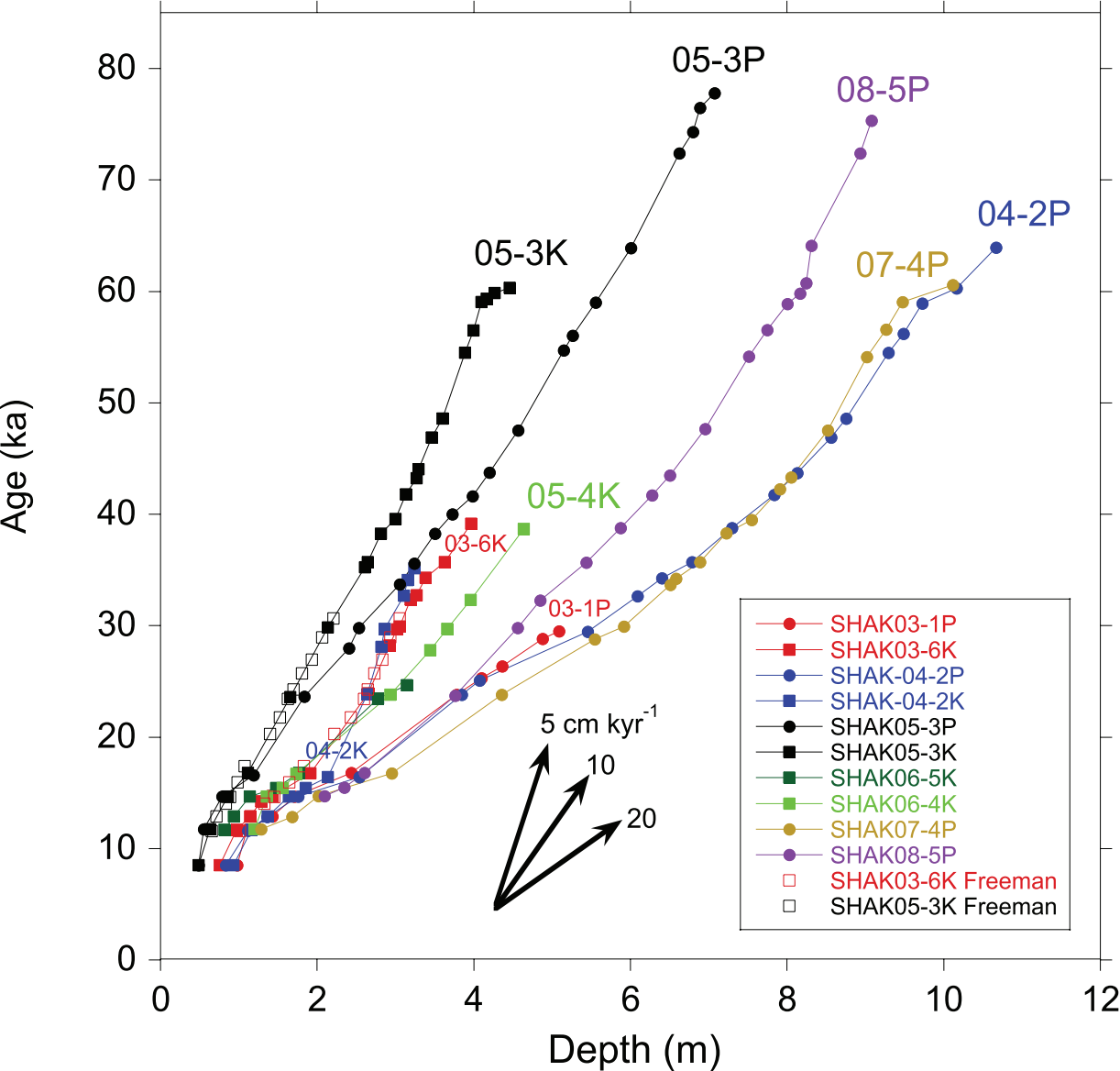
Age (ka)
Depth (m)
0
10
20
30
40
50
60
70
80
0
2
4
6
8
10
12
05-3P
08-5P
04-2P
07-4P
05-3K
05-4K
03-6K
03-1P
04-2K
5 cm kyr-1
10
20
SHAK03-1P
SHAK03-6K
SHAK-04-2P
SHAK-04-2K
SHAK05-3P
SHAK05-3K
SHAK06-5K
SHAK06-4K
SHAK07-4P
SHAK08-5P
SHAK03-6K Freeman
SHAK05-3K Freeman

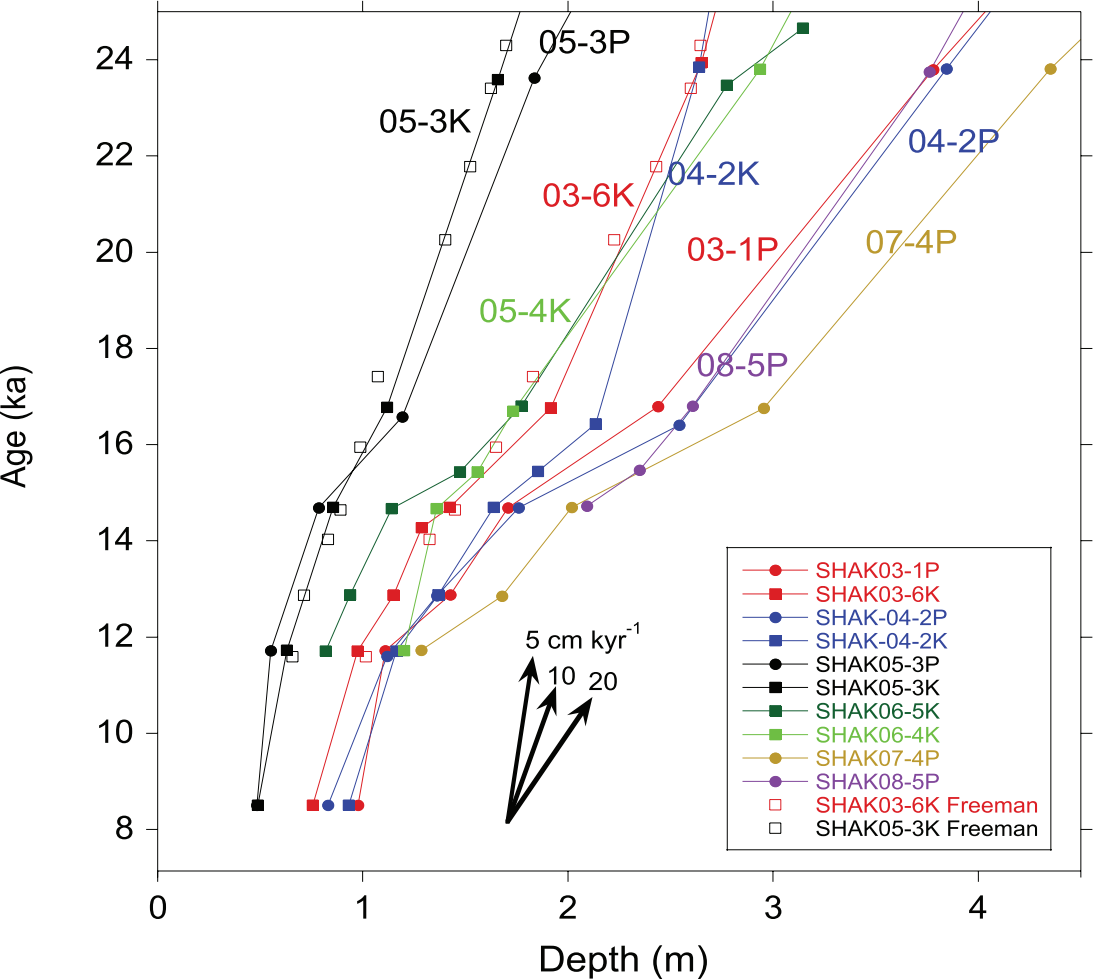
Age (ka)
Depth (m)
24
22
20
18
16
14
12
10
8
0
1
2
3
4
05-3P
05-3K
03-6K
04-2K
04-2P
03-1P
07-4P
05-4K
08-5P
5 cm kyr-1
10
20
SHAK03-1P
SHAK03-6K
SHAK-04-2P
SHAK-04-2K
SHAK05-3P
SHAK05-3K
SHAK06-5K
SHAK06-4K
SHAK07-4P
SHAK08-5P
SHAK03-6K Freeman
SHAK05-3K Freeman

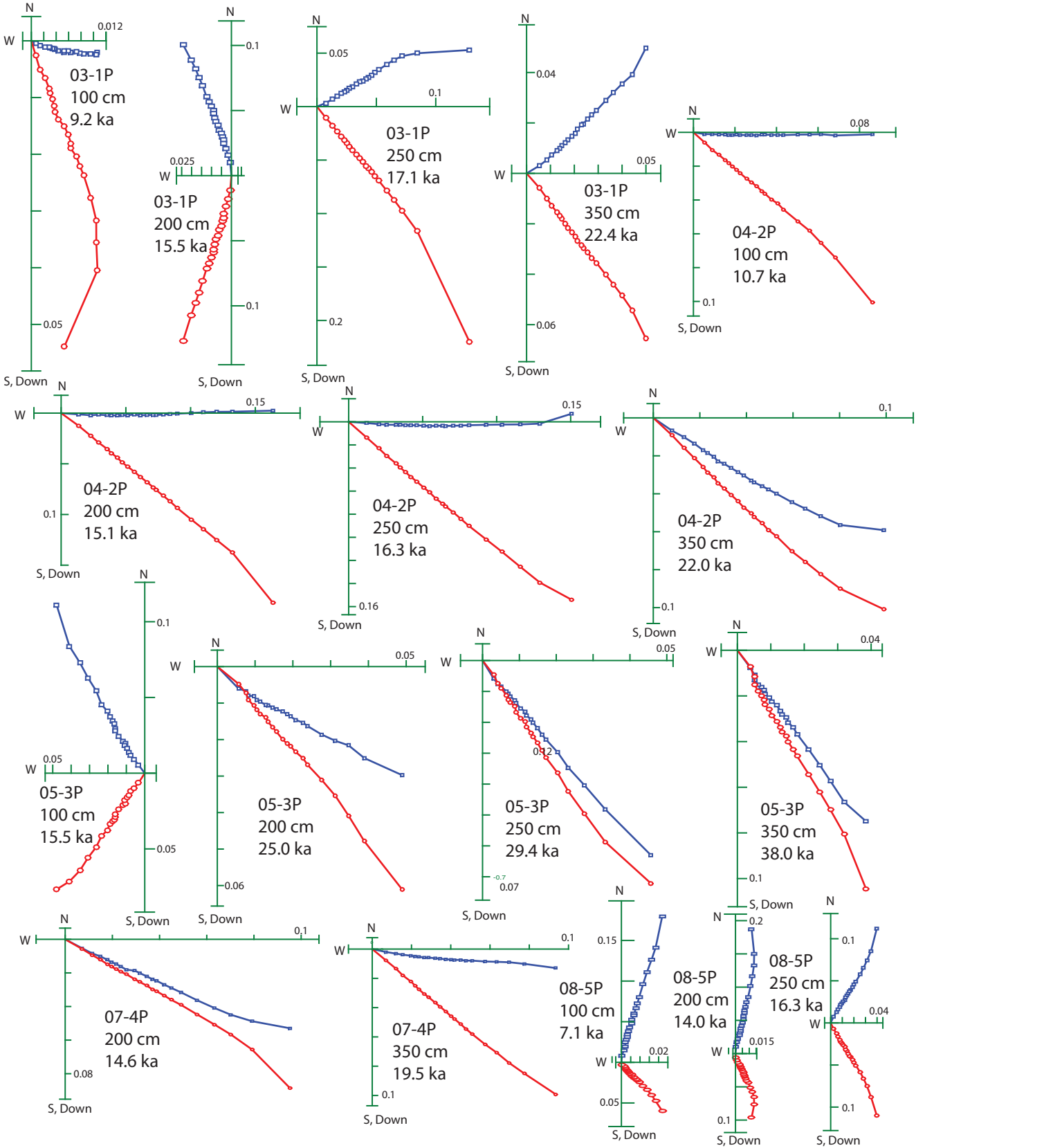
03-1P
100 cm
9.2 ka
03-1P
200 cm
15.5 ka
03-1P
250 cm
17.1 ka
03-1P
350 cm
22.4 ka
04-2P
100 cm
10.7 ka
04-2P
200 cm
15.1 ka
04-2P
250 cm
16.3 ka
04-2P
350 cm
22.0 ka
05-3P
100 cm
15.5 ka
05-3P
200 cm
25.0 ka
05-3P
250 cm
29.4 ka
05-3P
350 cm
38.0 ka
07-4P
200 cm
14.6 ka
07-4P
350 cm
19.5 ka
08-5P
100 cm
7.1 ka
08-5P
200 cm
14.0 ka
08-5P
250 cm
16.3 ka
N
W
S, Down

Table 1. JC089 cores included in the SW Iberian Margin stack

Station (Fig. 2)	Core	Core type	Lat. (°N)	Long. (°W)	WD (m)	Max. age (ka)	Recovery (m)	Mean sed. rate 10-45 ka (cm/kyr)
3	03-6K	Kasten	37.71	10.49	3740	41	4.16	10.2
3	03-1P	Piston	37.71	10.49	3731	30	5.14	17.2
4	04-2K	Kasten	37.59	10.36	3459	35	3.25	9.25
4	04-2P	Piston	37.59	10.36	3470	>45	10.69	18.3
5	05-3K	Kasten	37.60	10.69	4690	>45	4.68	7.5
5	05-3P	Piston	37.60	10.69	4662	>45	7.45	9.8
6	06-4K	Kasten	37.56	10.14	2646	40	4.75	12.2
6	06-5K	Kasten	37.56	10.14	2646	26	3.44	12.8
7	07-4P	Piston	37.85	10.15	3100	>45	10.19	18.4
8	08-5P	Piston	37.78	10.05	2619	>45	9.20	15.1

Table 2. Records other than from JC089 (Table 1) included in the RPI stacks for 0-45 ka

Site	Core type	Lat. (°)	Long. (°)	Water depth (m)	Mean sed rate (10-45 ka) cm/kyr	Ref.
MD01-2444 (SW Iberia)*	CAL	37.6 N	10.1 W	~3162	28	1
Portuguese Margin Stack*	CAL	39.0 N	10.2 W	2344	~25	2
Lac du Bouchet (France)	LC	4.9 N	3.8 E		22.2	3
Lake Biwa (Japan)	PC	35.2 N	136.1 E	67	40	4
Lake Potrok Aike (Patagonia)	PC	52.0 S	70.4 W	100	66	5
Lake Van (Turkey)	PC	38.6 N	42.7 E	360	40	6
Lake Towuti (Indonesia)	KPC	2.8 S	121.5 E	154	19	7
Black Sea	GC	42.0 N	37.0 E	200-800	60	8
MD04-2822 (Rockall Trough)	PC	56.8 N	11.4 W	2637	54	9
ODP 1063 (Bermuda Rise)	APC	33.7 N	57.6 W	4584	61	10
CH88-10p (Bermuda Rise)	PC	29.6 N	19.3 W	3818	23	11
MD98-2181 (Philippines)	CAL	6.3 N	125.8 E	2114	43	12
ODP 1089 (South Atlantic)	APC	40.9 S	9.9 E	4620	20	13
PS67-197-1 (Scotia Sea)	PC	55.1 S	44.1 W	3837	31	14

* included in SW Iberian Margin stack

Core type: LC Livingstone corer; KPC Kullenberg piston corer; PC piston corer; GC gravity corer; CAL Calypso corer (MD), APC Advanced piston corer (ODP).

References: (1) Channell et al. (2013), (2) Thouveny et al. (2004), (3) Thouveny et al. (1993), (4) Hayashida et al. (2007); (5) Lisé-Pronovost et al. (2013); (6) Vigilotti et al. (2014), (7) Kirana et al. (2018), (8) Nowaczyk et al. (2013), (9) Channell et al. (2016), (10) Channell et al. (2012), (11) Schwartz et al. (1996), (12) Stott et al. (2002), (13) Stoner et al. (2003), (14) Xiao et al. (2016).

Age (ka)	VADM ($x10^{22}$ Am^2)	Std. error		Age (ka)	VADM ($x10^{22}$ Am^2)	Std. error
4.00	6.585	0.592		25.00	10.136	0.478
4.50	6.604	0.585		25.50	9.833	0.537
5.00	7.032	0.541		26.00	9.800	0.450
5.50	6.432	0.391		26.50	8.600	0.648
6.00	6.777	0.354		27.00	9.112	0.538
6.50	6.162	0.522		27.50	8.257	0.520
7.00	5.705	0.391		28.00	9.283	0.462
7.50	5.625	0.350		28.50	8.627	0.389
8.00	5.587	0.343		29.00	8.384	0.430
8.50	5.284	0.334		29.50	7.926	0.396
9.00	5.708	0.417		30.00	8.581	0.360
9.50	6.728	0.655		30.50	9.119	0.419
10.00	7.238	0.728		31.00	9.601	0.535
10.50	6.798	0.374		31.50	10.386	0.445
11.00	6.881	0.308		32.00	10.695	0.587
11.50	7.380	0.355		32.50	9.746	0.620
12.00	8.573	0.725		33.00	9.533	0.636
12.50	9.179	0.835		33.50	9.533	0.472
13.00	8.303	0.703		34.00	7.120	0.566
13.50	8.078	0.847		34.50	7.016	0.452
14.00	8.731	0.641		35.00	7.346	0.335
14.50	8.830	0.764		35.50	8.984	0.481
15.00	10.615	0.646		36.00	8.483	0.430
15.50	11.935	0.828		36.50	7.497	0.326
16.00	12.676	0.796		37.00	6.617	0.327
16.50	12.309	0.647		37.50	6.758	0.409
17.00	13.101	0.667		38.00	6.847	0.497
17.50	13.593	0.569		38.50	6.719	0.425
18.00	14.267	0.570		39.00	5.875	0.450
18.50	13.356	0.632		39.50	5.326	0.450
19.00	11.847	0.613		40.00	4.006	0.329
19.50	12.314	0.387		40.50	2.639	0.356
20.00	12.867	0.458		41.00	2.354	0.201
20.50	12.756	0.396		41.50	3.244	0.270
21.00	12.537	0.378		42.00	4.045	0.296
21.50	11.528	0.359		42.50	5.612	0.331
22.00	10.918	0.435		43.00	6.472	0.369
22.50	10.462	0.555		43.50	7.964	0.467
23.00	10.823	0.476		44.00	7.942	0.570
23.50	10.752	0.503		44.50	7.970	0.568
24.00	9.744	0.389		45.00	8.266	0.494
24.50	10.034	0.462				

Age (ka)	^{10}Be-based intensity	Age (ka)	^{10}Be-based intensity
0.50	1.098	23.00	1.068
1.00	1.163	23.50	1.158
1.50	1.234	24.00	1.186
2.00	1.278	24.50	1.146
2.50	1.270	25.00	1.077
3.00	1.211	25.50	1.011
3.50	1.133	26.00	0.960
4.00	1.066	26.50	0.921
4.50	1.019	27.00	0.897
5.00	0.985	27.50	0.900
5.50	0.949	28.00	0.944
6.00	0.904	28.50	1.028
6.50	0.862	29.00	1.120
7.00	0.841	29.50	1.166
7.50	0.858	30.00	1.143
8.00	0.910	30.50	1.097
8.50	0.973	31.00	1.085
9.00	1.004	31.50	1.124
9.50	0.978	32.00	1.170
10.00	0.918	32.50	1.145
10.50	0.871	33.00	1.026
11.00	0.865	33.50	0.894
11.50	0.901	34.00	0.825
12.00	0.953	34.50	0.844
12.50	0.981	35.00	0.937
13.00	0.967	35.50	1.031
13.50	0.935	36.00	1.014
14.00	0.928	36.50	0.885
14.50	0.977	37.00	0.750
15.00	1.094	37.50	0.673
15.50	1.262	38.00	0.657
16.00	1.428	38.50	0.663
16.50	1.523	39.00	0.635
17.00	1.529	39.50	0.552
17.50	1.487	40.00	0.452
18.00	1.442	40.50	0.386
18.50	1.410	41.00	0.377
19.00	1.370	41.50	0.427
19.50	1.295	42.00	0.533
20.00	1.179	42.50	0.673
20.50	1.049	43.00	0.820
21.00	0.945	43.50	0.943
21.50	0.892	44.00	1.018
22.00	0.900	44.50	1.031
22.50	0.966	45.00	0.991